

Resolving magnon number states in quantum magnonics

Dany Lachance-Quirion,^{1,2,*} Yutaka Tabuchi,² Seiichiro Ishino,² Atsushi Noguchi,² Toyofumi Ishikawa,² Rekishu Yamazaki,² and Yasunobu Nakamura^{2,3,†}

¹*Institut quantique and Département de Physique,
Université de Sherbrooke, J1K 2R1, Sherbrooke, Québec, Canada*
²*Research Center for Advanced Science and Technology (RCAST),
The University of Tokyo, Meguro-ku, Tokyo 153-8904, Japan*

³*Center for Emergent Matter Science (CEMS), RIKEN, Wako, Saitama 351-0198, Japan*
(Dated: October 4th 2016)

Collective excitation modes in solid state systems play a central role in circuit quantum electrodynamics^{1,2}, cavity optomechanics³, and quantum magnonics^{4,5}. In the latter, quanta of collective excitation modes in a ferromagnet, called magnons, interact with qubits to provide the nonlinearity necessary to access quantum phenomena in magnonics. A key ingredient for future quantum magnonics systems is the ability to probe magnon states. Here we observe individual magnons in a millimeter-sized ferromagnet coherently coupled to a superconducting qubit. Specifically, we resolve magnon number states in spectroscopic measurements of a transmon qubit with the hybrid system in the strong dispersive regime^{6,7}. This enables us to detect a change in the magnetic dipole of the ferromagnet equivalent to a single spin flipped among more than 10^{19} spins. The strong dispersive regime of quantum magnonics opens up the possibility of encoding superconducting qubits into non-classical magnon states^{8,9}, potentially providing a coherent interface between a superconducting quantum processor and optical photons¹⁰⁻¹⁴.

Cavity and circuit quantum electrodynamics have enabled the realization of many gedanken experiments in quantum optics¹⁵⁻¹⁷, as well as offering a promising platform for quantum computing^{18,19}. Ideas from these fields have been applied to cavity optomechanics^{3,20,21}, with phonons in mechanical resonators, and quantum magnonics⁵, with magnons in magnetostatic modes. The coherent interaction between magnons and a superconducting qubit was demonstrated through the observation of a magnon-vacuum Rabi splitting of the qubit⁴. While this experiment was performed when both systems are resonantly coupled, here we go further and explore the off-resonant, dispersive regime of quantum magnonics, a promising regime to probe magnon states with the qubit.

To this end, we use an hybrid system which consists of a superconducting qubit and a single-crystalline yttrium iron garnet (YIG) sphere inside a three-dimensional microwave cavity (Fig. 1a). The transmon-type superconducting qubit has a resonant frequency of 7.9905 GHz. A pair of permanent magnets and a coil are used to apply a magnetic field B to the YIG sphere, making it a single-domain ferromagnet. The electric dipole of the qubit and

the magnetic dipole of the ferromagnet couple to the electric and magnetic fields of the cavity modes, respectively. The YIG sphere is placed near the anti-node of the magnetic field of the transverse electric TE₁₀₂ cavity mode, so that the cavity field is nearly uniform throughout the 0.5-mm sphere. This makes the uniformly-precessing mode, or Kittel mode, the most dominantly coupled magnetostatic mode. The interaction strength g_{m-c} between the TE₁₀₂ cavity mode, or coupler mode, and the Kittel mode reaches the strong coupling regime²²⁻²⁶, where $g_{m-c}/2\pi = 22.5$ MHz is much larger than both the cavity and magnon linewidths, respectively $\kappa_c/2\pi = 2.08$ MHz and $\gamma_m/2\pi = 1.3$ MHz (Supplementary Information).

The coupling of the superconducting qubit and the Kittel mode to the same cavity modes creates an effective interaction between these two macroscopic systems^{4,5}. To verify that this interaction is coherent, we perform spectroscopic measurements of the qubit with the hybrid system in the quantum regime at a temperature of 10 mK. While the qubit-magnon coupling is mostly provided by the TE₁₀₂ cavity mode at 8.4563 GHz (coupler mode), we use the dispersive interaction of the qubit with the TE₁₀₃ cavity mode at 10.4492 GHz (probe mode) for reading out the qubit (Fig. 1b). This scheme avoids measurement-induced dephasing caused by photon number fluctuations in the coupler mode^{5,6}. The change in the reflection coefficient r of a probe microwave tone, resonant with the probe mode and containing less than one photon on average, is measured while exciting the qubit with a spectroscopic microwave tone at frequency ω_s . Figure 1c shows the real part of the change of the reflection coefficient, Δr , measured for different currents I in the coil, changing the frequency $\omega_m \propto B$ of the magnons in the Kittel mode. The avoided crossing indicates the coherent interaction between the qubit and the Kittel mode⁴. Indeed, the qubit-magnon coupling strength g_{q-m} of 7.79 MHz, obtained from the magnon-vacuum Rabi splitting of the qubit (Fig. 1d), is much larger than both the power-broadened qubit linewidth $\gamma_q/2\pi = 1.74$ MHz and the magnon linewidth $\gamma_m/2\pi = 1.3$ MHz.

We now investigate the dispersive regime of our hybrid system, where the detuning between the bare qubit and Kittel mode frequencies, $|\omega_q^{\text{bare}} - \omega_m^{\text{bare}}|$, is much larger than g_{q-m} . The exchange of quanta of excitations between the qubit and the Kittel mode, through virtual photons in the coupler cavity mode, is then highly sup-

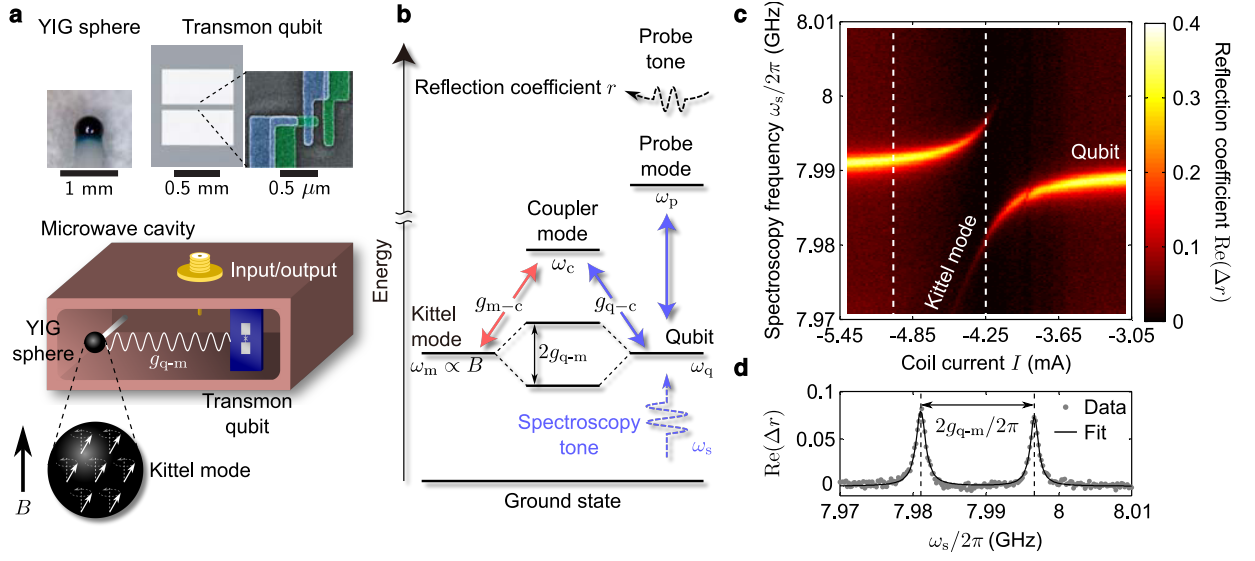


Figure 1. Hybrid system and qubit-magnon coherent interaction. **a**, Schematic illustration of a yttrium iron garnet (YIG) sphere and a superconducting transmon qubit inside a three-dimensional microwave cavity. A magnetic field B is applied to the YIG sphere using permanent magnets and a coil. The magnetostatic mode in which spins precess uniformly in the ferromagnetic sphere, or the Kittel mode, couples to the magnetic field of the cavity modes. The Kittel mode and the transmon qubit interact through virtual excitations in the cavity modes at a rate g_{q-m} . **b**, Schematic energy diagram of the coupler and probe cavity modes, the qubit, and the Kittel mode, respectively of frequencies ω_c , ω_p , ω_q , and ω_m . The qubit and the Kittel mode are coupled to the coupler cavity mode through electric and magnetic dipole interactions, at rates g_{q-c} and g_{m-c} , respectively. The spectrum of the qubit is measured by probing reflection of a microwave excitation, resonant with the probe mode at frequency ω_p , as a function of the spectroscopy frequency ω_s . **c**, Measurement of the qubit spectrum by probing the change of the reflection coefficient, $\text{Re}(\Delta r)$, as a function of the spectroscopy frequency ω_s and coil current I , changing the magnetic field at the YIG sphere. The avoided crossing indicates a coherent interaction between the qubit and the Kittel mode. Vertical dashed lines indicate $I = -4.25$ mA, where the qubit and the Kittel mode are hybridized (Fig. 1d), and $I = -5.02$ mA, where the qubit-magnon interaction is in the dispersive regime (Figs. 2 and 3). **d**, Magnon-vacuum Rabi splitting of the qubit on resonance with the Kittel mode at $I = -4.25$ mA. From the fit, we extract the qubit-magnon coupling rate $g_{q-m}/2\pi = 7.79$ MHz.

pressed. The dispersive part of the qubit-magnon Hamiltonian is then given by

$$\hat{\mathcal{H}}_{q-m}^{\text{disp}} = \hbar\chi_{q-m}\hat{\sigma}_z\hat{c}^\dagger\hat{c}, \quad (1)$$

where $\hat{\sigma}_z = |e\rangle\langle e| - |g\rangle\langle g|$, with $|g(e)\rangle$ the ground (excited) state of the transmon qubit, \hat{c}^\dagger (\hat{c}) is the magnon creation (annihilation) operator, and χ_{q-m} is the qubit-magnon dispersive shift^{1,5}. This dispersive interaction makes the qubit and magnon frequencies dependent on the state of the other system. More precisely, the qubit frequency $\omega_q^{(n_m)}$ depends on the magnon number state $|n_m\rangle = \{0, 1, 2, \dots\}$ and the magnon frequency ω_m^i depends on the transmon state $|i\rangle = \{g, e, f, \dots\}$. As illustrated in Fig. 2a, the strong dispersive regime, where $|2\chi_{q-m}| > \max[\gamma_q, \gamma_m]$, enables the observation of magnon number states $|n_m\rangle$ via magnon-number-dependent ac Stark shift of the qubit frequency when the Kittel mode is coherently driven^{6,7}. Figure 2b shows the dispersive shift χ_{q-m} expected for our hybrid system as a function of the dressed magnon frequency ω_m^g . The straddling regime, where we perform the spectroscopic study, corresponds to $\omega_q + \alpha < \omega_m^g < \omega_q$, where ω_q is the qubit frequency with the Kittel mode in the vacuum state. The transmon anharmonicity, $\alpha/2\pi = -120.2$ MHz, is defined

with $\omega_q + \alpha$ as the transition frequency between the $|e\rangle$ and $|f\rangle$ states of the transmon^{27,28} (Supplementary Information).

As illustrated in Fig. 2a, the qubit-magnon dispersive regime is investigated through spectroscopic measurements of the qubit while exciting the Kittel mode at frequency ω_{mw} , detuned by $\Delta_{\text{mw}} = \omega_m^g - \omega_{\text{mw}}$ from the dressed magnon frequency ω_m^g . The measurement of the qubit spectrum while sweeping ω_{mw} for a coil current of -5.02 mA and a Kittel mode excitation power P_{mw} of 7.9 fW is shown in Fig. 2c. Near resonant excitation $\Delta_{\text{mw}} \sim 0$, the qubit is ac Stark shifted by the magnon occupancy in the Kittel mode, a signature of the qubit-magnon dispersive interaction similar to the qubit-photon counterpart in circuit QED experiments^{6,29}. The positive magnon-induced ac Stark shift shows that $\chi_{q-m} > 0$, while the excitation frequency producing the maximum shift indicates $\omega_m^g/2\pi \approx 7.95$ GHz. Both these features are consistent with the hybrid system being in the straddling regime for $I = -5.02$ mA (Fig. 2b). More importantly, the peak corresponding to the qubit $|g\rangle \leftrightarrow |e\rangle$ transition with a *single* magnon in the Kittel mode, shifted from the zero-magnon qubit transition by $2\chi_{q-m} + \Delta_{\text{mw}}$, is visible at large de-

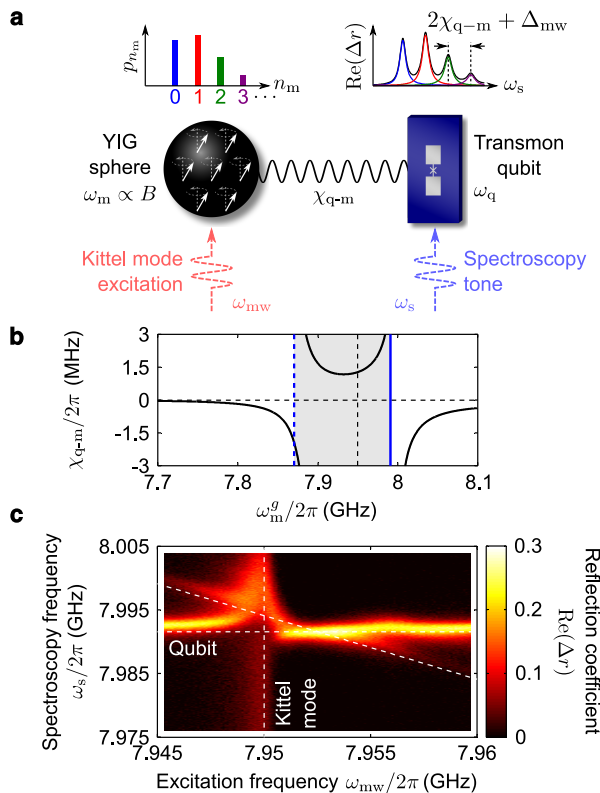


Figure 2. Dispersive qubit-magnon interaction. **a**, Schematic illustration of the hybrid system in the strong dispersive regime. A microwave excitation at frequency ω_{mw} is used to create a magnon coherent state in the Kittel mode. The excitation is detuned from the magnon frequency with the qubit in the ground state, ω_m^g , by $\Delta_{mw} = \omega_m^g - \omega_{mw}$. In the strong dispersive regime, magnon number states $|n_m\rangle$ (of probability distribution p_{n_m}) are mapped into the qubit spectrum as peaks at frequencies $\omega_q^{(n_m)}$, separated by $2\chi_{q-m} + \Delta_{mw}$ and with a spectral weight closely related to p_{n_m} . **b**, Calculation of the qubit-magnon dispersive shift χ_{q-m} as a function of the magnon frequency with the qubit in the ground state, ω_m^g . The straddling regime (shaded area) corresponds to ω_m^g between the transmon $|g\rangle \leftrightarrow |e\rangle$ transition frequency (ω_q , blue solid line) and $|e\rangle \leftrightarrow |f\rangle$ transition frequency ($\omega_q + \alpha$, blue dashed line, where $\alpha (< 0)$ is the transmon anharmonicity) with the Kittel mode in the vacuum state. **c**, Measurement of the qubit spectrum for a coil current $I = -5.02$ mA as a function of the Kittel mode excitation frequency ω_{mw} and the spectroscopy frequency ω_s . The excitation frequency producing the maximum magnon-induced ac Stark shift of the qubit from ω_q (horizontal dashed line) yields an estimation of $\omega_m^g/2\pi \approx 7.95$ GHz (vertical dashed line) for $I = -5.02$ mA. The Kittel mode spectrum, measured via its dispersive interaction with the probe mode, appears as a faint vertical line at ~ 7.95 GHz. Finally, the qubit transition frequency with a single magnon in the Kittel mode is shown as a diagonal dashed line calculated with the expected value $\chi_{q-m}/2\pi = 1.27$ MHz at $\omega_m^g/2\pi = 7.95$ GHz (vertical dashed line in **b**).

tunings.

We now focus on resolving magnon number states

through measurements with the excitation frequency close to resonance with the Kittel mode ($\Delta_{mw} \ll \gamma_m$). In the qubit spectra shown in Figs. 3a and 3b, the excitation frequency is fixed at 7.95 GHz, close to resonance with ω_m^g for $I = -5.02$ mA (Fig. 2c). The microwave excitation creates a magnon coherent state in the Kittel mode. Indeed, when coherently driving the Kittel mode, we observe peaks in the qubit spectrum at frequencies higher than the zero-magnon peak. These peaks correspond to different number of magnons in the Kittel mode.

To fit the data, we use an analytical model of the spectrum of a qubit dispersively coupled to a harmonic oscillator⁶. The asymmetric qubit lineshape at $P_{mw} = 0$ is well reproduced by including in the fit the photonic contribution to the qubit lineshape from the dispersive interaction between the qubit and the probe mode (Supplementary Information). The fitting parameters for each excitation power are the occupancy of the Kittel mode $\bar{n}_m^g = \langle \hat{n}_m \hat{\Pi}_q^g \rangle$, where $\hat{\Pi}_q^g = |g\rangle\langle g|$ is the projector to the qubit ground state, the qubit-magnon dispersive shift, χ_{q-m} , and the excitation detuning, Δ_{mw} (Figs. 3a and 3c). We find a detuning Δ_{mw} of -0.38 MHz, indicating a bare magnon frequency ω_m^{bare} of 7.9515 GHz (Supplementary Information). The condition for the dispersive regime is therefore clearly respected with a detuning $|\omega_q^{\text{bare}} - \omega_m^{\text{bare}}|$ of 89 MHz much larger than the qubit-magnon coupling strength. The qubit-magnon dispersive shift χ_{q-m} is found to be 1.5 ± 0.1 MHz, in good agreement with the theoretical value of 1.27 MHz (Fig. 2b). Resolving magnon number states clearly demonstrates that we have reached the strong dispersive regime of quantum magnonics, with the dispersive shift per magnon $2\chi_{q-m}$ larger than both the power-broadened qubit linewidth $\gamma_q/2\pi = 0.78$ MHz and the magnon linewidth $\gamma_m/2\pi = 1.3$ MHz.

The average number of magnons \bar{n}_m^g in the Kittel mode extracted from the fit of the data is shown in Fig. 3d. At the lowest excitation power of 79 aW, we are able to resolve 0.026 ± 0.012 magnons in the Kittel mode of the ferromagnetic sphere containing about 1.4×10^{18} spins. This is therefore a change in magnetic dipole equivalent to a single spin flipped among $\sim 5 \times 10^{19}$ spins. Within our resolution of about 0.01 magnons, no thermal occupancy of the Kittel mode is observed, indicating that the millimeter-sized ferromagnet is indeed in its magnon-vacuum state. Furthermore, the nonlinearity of \bar{n}_m^g against the excitation power can be explained by a Kerr nonlinearity in the Kittel mode caused by the anharmonicity of the transmon^{17,30}. We find a Kerr coefficient of -0.20 ± 0.09 MHz, in good agreement with the expected value of -0.12 MHz (Supplementary Information).

Finally, we compute the probability p_{n_m} of having n_m magnons in the Kittel mode with

$$p_{n_m} = \int d\omega_s S_{n_m}(\omega_s) / S(\omega_s), \quad (2)$$

where $S(\omega_s) \approx \sum_{n_m=0}^{10} S_{n_m}(\omega_s)$ is the qubit spectrum in the analytical model, to which data is fitted, and $S_{n_m}(\omega_s)$

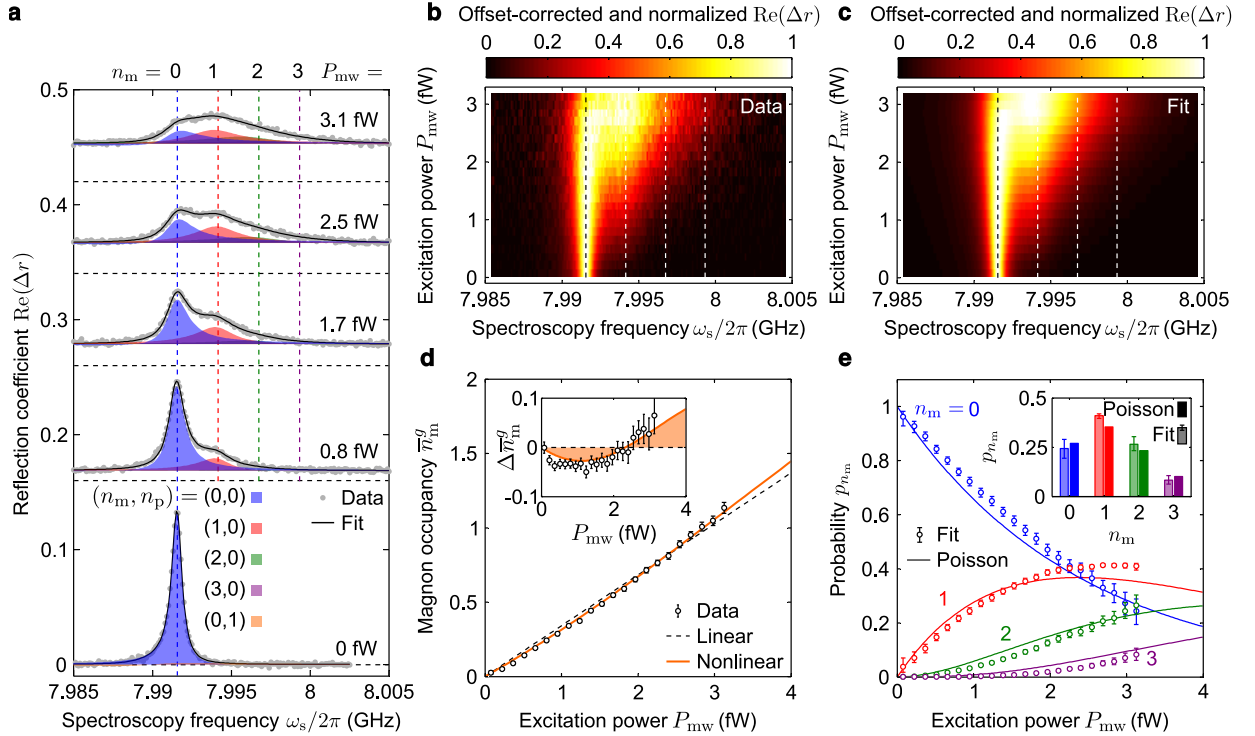


Figure 3. Resolving magnon number states. **a**, Measurements of the qubit spectrum at different Kittel mode excitation powers P_{mw} for a coil current of -5.02 mA and Kittel mode excitation frequency of 7.95 GHz. Black lines show fits of the data to the spectrum of a qubit dispersively coupled to a harmonic oscillator. Color-coded shaded areas show components of the spectrum corresponding to different photon number states $|n_p\rangle$ of the probe cavity mode and magnon number states $|n_m\rangle$. Vertical offsets are shown by horizontal dashed lines. **b**, Measured and **c**, fitted qubit spectra as a function of P_{mw} . For clarity, after subtracting a power-dependent offset, $\text{Re}(\Delta r)$ is normalized relative to its maximum for each drive power. For **a**, **b** and **c**, vertical dashed lines indicate the frequencies $\omega_q^{(n_m)}$ of the dressed qubit $|g\rangle \leftrightarrow |e\rangle$ transitions corresponding to the first four magnon number states. **d**, Magnon occupancy \bar{n}_m^g as a function of the excitation power. Dashed black line and solid orange line show fits to a driven linear and nonlinear Kittel mode, respectively. Inset: Deviations $\Delta\bar{n}_m^g$ from the linear fit, indicating a significant magnon Kerr nonlinearity. **e**, Probability p_{n_m} of the first four magnon number states as a function of P_{mw} . Poisson distributions are shown as solid lines. Inset: p_{n_m} for $P_{\text{mw}} = 3.1$ fW. For both **d** and **e**, error bars correspond to 95% confidence intervals.

is its component associated with the magnon number state $|n_m\rangle$. For $2\chi_{q-m} \gg \gamma_m$, the probability distribution calculated with equation (2) falls back to the Poisson distribution expected for a driven harmonic oscillator⁶ (Supplementary Information). The probability distributions p_{n_m} of the first four magnon number states, shown in Fig. 3e, indicate small deviations from Poisson distributions. This is expected as the qubit-magnon dispersive shift is only slightly larger than the magnon linewidth in our hybrid system. Nevertheless, our ability to map the probability distribution of magnon number states to the spectrum of a qubit provides a novel tool to investigate quantum states in magnetostatic modes.

Looking forward, the strong dispersive interaction between magnons and a superconducting qubit demon-

strated here should enable the encoding of the qubit into a superposition of magnon coherent states in a magnetostatic mode^{8,9}. However, to implement this encoding protocol, the qubit-magnon system needs to be deeper into the strong dispersive regime, either by increasing the qubit-magnon coupling strength or by decreasing the magnon linewidth in the quantum regime²³. Together with the recently demonstrated bidirectional conversion between microwave and optical photons in yttrium iron garnet¹², this could pave the way to the transfer of quantum states between superconducting qubits and photons in optical fibers. Combining two very promising candidates for both stationary and flying qubits, such a breakthrough would be an important step toward the realization of a superconducting qubit-based quantum network.

* dany.lachance.quirion@usherbrooke.ca

† yasunobu@qc.rcast.u-tokyo.ac.jp

¹ Blais, A. *et al.* Cavity quantum electrodynamics for superconducting electrical circuits: An architecture for quantum

- computation. *Phys. Rev. A*, **69**, 062320 (2004).
- ² Wallraff, A. *et al.* Strong coupling of a single photon to a superconducting qubit using circuit quantum electrodynamics. *Nature*, **431**, 162-167 (2004).
 - ³ Aspelmeyer, M., Kippenberg, T. J. & Marquardt, F. Cavity optomechanics. *Rev. Mod. Phys.*, **86**, 1391-1452 (2014).
 - ⁴ Tabuchi, Y. *et al.* Coherent coupling between a ferromagnetic magnon and a superconducting qubit. *Science*, **349**, 405-408 (2015).
 - ⁵ Tabuchi, Y. *et al.* Quantum magnonics: The magnon meets the superconducting qubit. *Comptes Rendus Physique*, **17**, 729-739 (2016).
 - ⁶ Gambetta, J. *et al.* Qubit-photon interactions in a cavity: Measurement-induced dephasing and number splitting. *Phys. Rev. A*, **74**, 042318 (2006).
 - ⁷ Schuster, D. I. *et al.* Resolving photon number states in a superconducting circuit. *Nature*, **445**, 515-518 (2007).
 - ⁸ Leghtas, Z. *et al.* Deterministic protocol for mapping a qubit to coherent state superpositions in a cavity. *Phys. Rev. A*, **87**, 042315 (2013).
 - ⁹ Vlastakis, B. *et al.* Deterministically encoding quantum information using 100-photon Schrödinger cat states. *Science*, **342**, 607-610 (2013).
 - ¹⁰ Kimble, H. J. The quantum internet. *Nature*, **453**, 1023-1030 (2008).
 - ¹¹ Osada, A. *et al.* Cavity optomagnonics with spin-orbit coupled photons. *Phys. Rev. Lett.*, **116**, 223601 (2016).
 - ¹² Hisatomi, R. *et al.* Bidirectional conversion between microwave and light via ferromagnetic magnons. *Phys. Rev. B*, **93**, 174427 (2016).
 - ¹³ Zhang, X., Zhu, N., Zou, Ch.-L. & Tang, H. X. Optomagnonic whispering gallery microresonators. *Phys. Rev. Lett.*, **117**, 123605 (2016).
 - ¹⁴ Haigh, J. A., Nunnenkamp, A., Ramsay, A. J. & Ferguson, A. J. Triple-resonant Brillouin light scattering in magneto-optical cavities. *Phys. Rev. Lett.*, **117**, 133602 (2016).
 - ¹⁵ Haroche, S. & Raimond, J.-M. Exploring the quantum. *Oxford University Press*, (2006).
 - ¹⁶ Hofheinz, M. *et al.* Synthesizing arbitrary quantum states in a superconducting resonator. *Nature*, **459**, 546-549 (2009).
 - ¹⁷ Kirchmair, G. *et al.* Observation of quantum state collapse and revival due to the single-photon Kerr effect. *Nature*, **495**, 205-209 (2013).
 - ¹⁸ Ladd, T. D. *et al.* Quantum computers. *Nature*, **464**, 45-53 (2010).
 - ¹⁹ Kelly, J. *et al.* State preservation by repetitive error detection in a superconducting quantum circuit. *Nature*, **519**, 66-69 (2015).
 - ²⁰ Teufel, J. D. *et al.* Circuit cavity electromechanics in the strong-coupling regime. *Nature*, **471**, 204-208 (2011).
 - ²¹ Lecocq, F. *et al.* Resolving the vacuum fluctuations of an optomechanical system using an artificial atom. *Nat. Phys.*, **11**, 635-639 (2015).
 - ²² Huebl, H., Zollitsch, C. & Lotze, J. High cooperativity in coupled microwave resonator ferrimagnetic insulator hybrids. *Phys. Rev. Lett.*, **111**, 127003 (2013).
 - ²³ Tabuchi, Y. *et al.* Hybridizing ferromagnetic magnons and microwave photons in the quantum limit. *Phys. Rev. Lett.*, **113**, 083603 (2014).
 - ²⁴ Goryachev, M. *et al.* High-cooperativity cavity QED with magnons at microwave frequencies. *Phys. Rev. Applied*, **2**, 054002 (2014).
 - ²⁵ Zhang, X. *et al.* Magnon dark modes and gradient memory. *Nat. Commun.*, **6**, 8914 (2015).
 - ²⁶ Lambert, N. J. *et al.* Cavity-mediated coherent coupling of magnetic moments. *Phys. Rev. A*, **93**, 021803(R) (2016).
 - ²⁷ Koch, J. *et al.* Charge-insensitive qubit design derived from the Cooper pair box. *Phys. Rev. A*, **76**, 042319 (2007).
 - ²⁸ Inomata, K. *et al.* Large dispersive shift of cavity resonance induced by a superconducting flux qubit in the straddling regime. *Phys. Rev. B*, **86**, 140508(R) (2012).
 - ²⁹ Schuster, D. I. *et al.* ac Stark shift and dephasing of a superconducting qubit strongly coupled to a cavity field. *Phys. Rev. Lett.*, **94**, 123602 (2005).
 - ³⁰ Bourassa, J., Beaudoin, F., Gambetta, J. M. & Blais, A. Josephson-junction-embedded transmission-line resonators: From Kerr medium to in-line transmon. *Phys. Rev. A*, **86**, 013814 (2012).

Acknowledgements

The authors acknowledge K. Usami, A. Blais, J. Bourassa, and M. Pioro-Ladrière for useful discussions and P.-M. Billangeon for fabricating the transmon qubit. This work was partly supported by the Project for Developing Innovation System of MEXT, JSPS KAKENHI (Grant Number 26600071, 26220601), NICT, ERATO, JST, the Murata Science Foundation, Research Foundation for Opto-Science and Technology, Tateisi Science and Technology Foundation, JSPS Summer Program, and the Natural Sciences and Engineering Research Council of Canada (NSERC).

Authors contributions

The measurements were carried out by D.L.-Q. and S.I., with input from all authors. D.L.-Q., Y.T., and Y.N. analysed the data and wrote the manuscript with input from all authors. Y.T., S.I., and Y.N. conceived the hybrid system with input from A.N., T.I., and R.Y.

Additional information

Supplementary information is available in the online version of the paper. Reprints and permissions information is available online at www.nature.com/reprints. Correspondence and requests for materials should be addressed to D.L.-Q. and Y.N.

Competing financial interests

The authors declare no competing financial interests.

Supplementary Information for “Resolving magnon number states in quantum magnonics”

Dany Lachance-Quirion,^{1,2} Yutaka Tabuchi,² Seiichiro Ishino,² Atsushi Noguchi,²
Toyofumi Ishikawa,² Rekishu Yamazaki,² and Yasunobu Nakamura^{2,3,*}

¹*Institut quantique and Département de Physique,
Université de Sherbrooke, J1K 2R1, Sherbrooke, Québec, Canada*

²*Research Center for Advanced Science and Technology (RCAST),
The University of Tokyo, Meguro-ku, Tokyo 153-8904, Japan*

³*Center for Emergent Matter Science (CEMS), RIKEN, Wako, Saitama 351-0198, Japan*

CONTENTS

I. Experimental setup and hybrid system	2
II. Hamiltonian of the hybrid system	2
III. Cavity-magnon coupling	3
IV. Qubit spectrum in the dispersive regime	3
V. Qubit spectroscopy - Magnon vacuum state	4
A. Measurement	4
B. Analytical model	5
C. Fit	5
VI. Qubit spectroscopy - Magnon coherent state	6
A. Analytical model and fit	6
B. Kittel mode excitation	7
C. Probability distribution	7
VII. Magnon Kerr nonlinearity	8
References	8

I. EXPERIMENTAL SETUP AND HYBRID SYSTEM

Figure S1 shows the instruments and components used in the experiment. Microwave powers P_r , P_s , and P_{mw} are calibrated using as the reference point the input of the cavity. At that reference point, the reflection coefficient r is unity when $|\omega_r - \omega_{10p}| \gg \kappa_{10p}$, where ω_r is the readout frequency, and ω_{10p} and κ_{10p} are the resonant frequency and the linewidth of the TE_{10p} cavity mode, respectively, with $p = 1, 2, 3 \dots$. Taking into account attenuation in cables outside and inside the dilution refrigerator, the total attenuation between the microwave sources and the input of the cavity are approximately 81 dB, 122 dB, and 121 dB for the readout, spectroscopy, and Kittel mode microwave excitations, respectively.

The yoke, coil, cavity and YIG sphere of the hybrid system used in the paper are the same as in Ref. [S1], while the transmon qubit is a different one. The oxygen-free copper microwave cavity has dimensions of $24 \times 3 \times 53$ mm³. A SMA connector connected to the cavity is used to measure the reflection coefficient r . A pair of disc-shape neodymium permanent magnets, with a diameter of 10 mm and a thickness of 1 mm each, are placed at the ends of a magnetic yoke made of pure iron. The magnets produce a static field $B \approx 0.29$ T in the 4-mm gap between them. The magnetic field can be additionally tuned by a current I in a 10^4 -turn superconducting coil. The field-to-current conversion ratio is approximately 1.7 mT/mA. A YIG sphere glued to an aluminium-oxide rod along the $\langle 110 \rangle$ crystal axis is mounted in the cavity at the center of the gap between the magnets. The static field is applied in parallel with the $\langle 100 \rangle$ crystal axis. A transmon-type superconducting qubit, consisting of two large-area aluminium pads and a single Josephson junction (Al/Al₂O₃/Al), is fabricated on a silicon substrate and is mounted inside the cavity. The qubit and the YIG sphere are separated by 35 mm in the horizontal direction. A double-layer magnetic shield made of aluminium and pure iron covers half of the cavity to protect the qubit from the stray magnetic field of the magnet.

II. HAMILTONIAN OF THE HYBRID SYSTEM

The Hamiltonian of the hybrid system is given by

$$\begin{aligned} \hat{\mathcal{H}}/\hbar = & \sum_{p=1}^{\infty} \omega_{10p}^{\text{bare}} \hat{a}_p^\dagger \hat{a}_p + (\omega_q^{\text{bare}} - \alpha^{\text{bare}}/2) \hat{b}^\dagger \hat{b} + (\alpha^{\text{bare}}/2) (\hat{b}^\dagger \hat{b})^2 + \omega_m^{\text{bare}} \hat{c}^\dagger \hat{c} \\ & + \sum_{p=1}^{\infty} \left(g_{q,10p} (\hat{a}_p^\dagger \hat{b} + \hat{a}_p \hat{b}^\dagger) + g_{m,10p} (\hat{a}_p^\dagger \hat{c} + \hat{a}_p \hat{c}^\dagger) \right), \end{aligned} \quad (\text{S1})$$

where $\omega_{10p}^{\text{bare}}$ is the bare frequency of the TE_{10p} mode of the cavity, $\omega_q^{\text{bare}} \equiv \omega_{ge}$ and ω_{ef} are, respectively, the bare frequencies of the $|g\rangle \leftrightarrow |e\rangle$ and $|e\rangle \leftrightarrow |f\rangle$ transitions of the transmon qubit, $\alpha^{\text{bare}} \equiv \omega_{ef} - \omega_{ge}$ is the bare anharmonicity of the transmon qubit, ω_m^{bare} is the bare magnon frequency, $g_{q,10p}$ is the coupling strength between the TE_{10p} cavity mode and the transmon qubit, and $g_{m,10p}$ is the coupling strength between the TE_{10p} cavity mode and the Kittel mode [S2]. In equation (S1), \hat{a}_p^\dagger (\hat{a}_p), \hat{b}^\dagger (\hat{b}), and \hat{c}^\dagger (\hat{c}) are the creation (annihilation) operators of, respectively, a photon in the TE_{10p} cavity mode, an excitation in the transmon qubit and a magnon in the Kittel mode. In the Hamiltonian of equation (S1), the transmon qubit is considered as an anharmonic oscillator in order to take into account the effect of the $|e\rangle \leftrightarrow |f\rangle$ transition on the values of the calculated parameters, therefore capturing the straddling regime of the qubit-magnon system [S3].

The parameters of the hybrid system in equation (S1) are shown in Table S1. We calculate values of the qubit-magnon coupling strength g_{q-m} , the qubit- TE_{103} cavity mode dispersive shift $\chi_{q,103}$, the qubit-magnon dispersive shift χ_{q-m} , and the magnon Kerr coefficient K_m using these parameters and the above Hamiltonian by truncating the sum over the TE_{10p} modes of the cavity to $p = 4$. We consider the TE_{10p} cavity mode number states $|n_{10p} = \{0, 1, 2\}\rangle$, the transmon states $|i = \{g, e, f\}\rangle$, and the Kittel mode magnon number states $|n_m = \{0, 1, 2\}\rangle$. More explicitly, we diagonalize the Hamiltonian and evaluate the parameters with

$$\begin{aligned} \chi_{q,103} &= \frac{1}{2} (\omega_{103}^e - \omega_{103}^g), \\ \chi_{q-m} &= \frac{1}{2} (\omega_m^e - \omega_m^g), \\ K_m &= 2\omega_{m,0 \rightarrow 1}^g - \omega_{m,0 \rightarrow 2}^g, \end{aligned}$$

where $\omega_{103}^{g(e)}$ is the frequency of the TE_{103} cavity mode with the transmon in the ground (excited) state, $\omega_m^{g(e)}$ is the frequency of the Kittel mode with the transmon in the ground (excited) state, and $\omega_{m,0 \rightarrow n_m}^g$ is the transition frequency

of the Kittel mode between the magnon vacuum state and the $|n_m\rangle$ magnon number state with the transmon in the ground state, with $\omega_m^g \equiv \omega_{m,0 \rightarrow 1}^g$, such that for $K_m = 0$, $\omega_{m,0 \rightarrow n_m}^g = n_m \omega_m^g$. The qubit-magnon interaction strength g_{q-m} is simply calculated by half the splitting in the qubit-magnon hybridized energy levels. Figure 2b in the main text shows the calculated qubit-magnon dispersive shift χ_{q-m} as a function of the dressed magnon frequency ω_m^g , while Fig. S6a shows the magnon Kerr coefficient K_m as a function of the bare magnon frequency ω_m^{bare} . Table S4 summarizes the theoretical values of g_{q-m} , $\chi_{q,103}$, χ_{q-m} , and K_m .

As in the main text, the TE_{102} and TE_{103} cavity modes are, from now on, labeled the coupler and probe cavity modes, respectively. Therefore, indices ‘102’ and ‘103’ are replaced by indices ‘c’ and ‘p’, respectively.

III. CAVITY-MAGNON COUPLING

Data on the avoided crossing between the TE_{102} cavity mode (coupler mode) and the Kittel mode is shown in Fig. S2a. Figure S2b shows the current-dependent dressed cavity frequency with the qubit in the ground state, $\omega_c^g(I)$, extracted from data of Fig. S2a. The dressed cavity frequency is fitted to

$$\omega_c^g(I) = p_1 I + p_2 - \text{sgn}(I - I_0) \sqrt{(p_1 I - p_3)^2 + p_4^2}, \quad (\text{S2})$$

with the fitting parameters p_1 to p_4 related to the physical quantities by

$$\begin{aligned} \omega_c^{\text{bare}'} &= p_2 + p_3, \\ \omega_m^{\text{bare}'}(I) &= (p_2 - p_3) + (2p_1) \times I, \\ |g_{m-c}| &= p_4, \\ \omega_m^{\text{bare}'}(I_0) &\equiv \omega_c^{\text{bare}'}. \end{aligned}$$

In the above equations, $\omega_c^{\text{bare}'}$ is the frequency of the coupler mode bare of its interaction with the Kittel mode, $\omega_m^{\text{bare}'}$ is the frequency of the Kittel mode bare of its interaction with the coupler mode, g_{m-c} is the coupling strength between the coupler mode and the Kittel mode, and I_0 is the coil current for which $\omega_m^{\text{bare}'} = \omega_c^{\text{bare}'}$. This enables us to determine $\omega_c^{\text{bare}'}/2\pi = 8.456$ GHz.

We furthermore fit the cavity spectrum $\text{Re}(r)$ to

$$\text{Re}(r) = \text{Re} \left(\frac{\omega_r - \omega_c^{\text{bare}'} + \frac{i(\kappa_c^{\text{int}} - \kappa_c^{\text{cpl}})}{2} - \frac{|g_{m-c}|^2}{\omega_r - \omega_m^{\text{bare}'}(I) + i\gamma_m/2}}{\omega_r - \omega_c^{\text{bare}'} + \frac{i\kappa_c}{2} - \frac{|g_{m-c}|^2}{\omega_r - \omega_m^{\text{bare}'}(I) + i\gamma_m/2}} \right), \quad (\text{S3})$$

where ω_r is the readout frequency, κ_c^{int} is the internal loss rate of the coupler mode, κ_c^{cpl} is the coupling rate of the input/output port to the coupler mode, $\kappa_c = \kappa_c^{\text{int}} + \kappa_c^{\text{cpl}}$ is the total linewidth of the coupler mode, and γ_m is the magnon linewidth [?]. Values of κ_c^{int} , κ_c^{cpl} , and κ_c , given in Table S2, are determined from a measurement of the coupler cavity mode spectrum far from the avoided crossing ($I = -10$ mA) while the value of $\omega_c^{\text{bare}'}$ is fixed by the fit of $\omega_c^g(I)$ to equation (S2). The global fitting parameters are γ_m and g_{m-c} while $\omega_m^{\text{bare}'}$ is fitted for each coil current I .

Figure S2c shows spectra fitted to equation (S3) for coil currents I near the avoided crossing at $I_0 \approx 5.5$ mA. We find $g_{m-c}/2\pi = 22.5 \pm 0.1$ MHz and $\gamma_m/2\pi = 1.3 \pm 0.3$ MHz, with error bars corresponding to 95% confidence intervals. The avoided crossing calculated with equation (S3) and the parameters determined from the above fits is shown in Fig. S2d.

IV. QUBIT SPECTRUM IN THE DISPERSIVE REGIME

The effective Hamiltonian of a driven qubit-harmonic oscillator system in the dispersive regime is given by

$$\hat{\mathcal{H}}/\hbar = \frac{1}{2} \Delta_s \hat{\sigma}_z + (\Delta_d + \chi) \hat{d}^\dagger \hat{d} + \chi \hat{\sigma}_z \hat{d}^\dagger \hat{d} + \Omega_s (\hat{\sigma}^- + \hat{\sigma}^+) + \Omega_d (\hat{d} + \hat{d}^\dagger), \quad (\text{S4})$$

where $\Delta_s = \omega_q - \omega_s$ is the spectroscopy detuning, ω_q is the qubit frequency with the oscillator in the vacuum state, ω_s is the spectroscopy excitation frequency, $\Delta_d = \omega_o^g - \omega_d$ is the drive detuning, $\omega_o^{g(e)}$ is the oscillator frequency with the qubit in the ground (excited) state, ω_d is the drive frequency, \hat{d}^\dagger (\hat{d}) is the creation (annihilation) operator of the

oscillator, χ is the dispersive shift, Ω_s is the spectroscopy excitation strength (Rabi frequency), Ω_d is the oscillator excitation strength. In equation (S4), the qubit and the oscillator are in the frames rotating at the qubit frequency ω_q and the oscillator frequency ω_o^g , respectively.

From the Hamiltonian of equation (S4), Gambetta *et al.* obtained an analytical expression for the qubit spectrum $S(\omega_s)$ [S4], given by

$$S(\omega_s) = \sum_{n=0}^{\infty} \frac{1}{\pi} \frac{1}{n!} \text{Re} \left(\frac{(-A)^n e^A}{\gamma_q^{(n)} - i(\omega_s - \omega_q^{(n)})} \right) \equiv \sum_{n=0}^{\infty} S_n(\omega_s), \quad (\text{S5})$$

with

$$\omega_q^{(n)} = \omega_q + B + n(2\chi + \Delta_d), \quad (\text{S6})$$

$$\gamma_q^{(n)} = \gamma_q + \kappa(n + D^{\text{ss}}), \quad (\text{S7})$$

$$A = D^{\text{ss}} \left(\frac{\kappa/2 - i(2\chi + \Delta_d)}{\kappa/2 + i(2\chi + \Delta_d)} \right), \quad (\text{S8})$$

$$B = \chi(\bar{n}^g + \bar{n}^e - D^{\text{ss}}), \quad (\text{S9})$$

$$D^{\text{ss}} = \frac{2(\bar{n}^g + \bar{n}^e)\chi^2}{(\kappa/2)^2 + \chi^2 + (\chi + \Delta_d)^2}, \quad (\text{S10})$$

$$\bar{n}^g = \frac{\Omega_d^2}{(\kappa/2)^2 + \Delta_d^2}, \quad (\text{S11})$$

$$\bar{n}^e = \frac{\Omega_d^2}{(\kappa/2)^2 + (\Delta_d + 2\chi)^2}. \quad (\text{S12})$$

In the above equations, $\omega_q^{(n)}$ and $\gamma_q^{(n)}$ are respectively the frequency and the linewidth of the qubit peak corresponding to the number state $|n\rangle$ and the steady-state distinguishability D^{ss} , and κ is the linewidth of the harmonic oscillator. The steady-state distinguishability D^{ss} is defined as the separation between the steady-state coherent states $|\alpha_{g,e}^{\text{ss}}\rangle$ created in the oscillator by the microwave excitation with the qubit in the ground state and the excited state, $D^{\text{ss}} = |\alpha_e^{\text{ss}} - \alpha_g^{\text{ss}}|^2$. The last term in equation (S7) shows that as the coherent states $|\alpha_{g,e}^{\text{ss}}\rangle$ become more distinguishable, the qubit linewidth $\gamma_q^{(n)}$ increases due to the measurement-induced dephasing [S4]. The occupancy with the qubit in the ground (excited) state is given by $\bar{n}^{g(e)} = |\alpha_{g(e)}^{\text{ss}}|^2 = \langle \hat{n} \hat{\Pi}_q^{g(e)} \rangle$, where $\hat{\Pi}_q^{g(e)} = |g(e)\rangle\langle g(e)|$ is the projector of the qubit to its ground (excited) state.

For $\chi \gg \kappa$ and $\Delta_d = 0$, the steady-state distinguishability D^{ss} is simply given by $D^{\text{ss}} = \bar{n}^g + \bar{n}^e$ and $A \rightarrow -D^{\text{ss}}$. In that case, the component of the qubit spectrum with n excitations, $S_n(\omega_s)$, has a Lorentzian lineshape. The qubit spectrum $S(\omega_s)$ is therefore well described by a sum of Lorentzian functions at frequencies $\omega_q^{(n)}$ and of linewidths $\gamma_q^{(n)}$ with a Poisson distributed spectral weight of mean given by D^{ss} . However, for $\chi \sim \kappa$, A becomes complex, leading to a non-Lorentzian lineshape for $S_n(\omega_s)$, with possibly negative values. However, the integral over ω_s of the spectrum and its components is positive in all cases.

V. QUBIT SPECTROSCOPY - MAGNON VACUUM STATE

A. Measurement

We perform spectroscopy of the qubit by probing the change Δr in the reflection coefficient r of a readout microwave excitation of fixed frequency ω_r as a function of the spectroscopy frequency ω_s . For all qubit spectroscopy measurements presented here, ω_r is fixed at the frequency of the dressed TE₁₀₃ cavity mode (probe mode) with the qubit in the ground state at $\omega_p^g/2\pi = 10.44916$ GHz such that $\Delta_r = \omega_p^g - \omega_r = 0$. The readout excitation power P_r is fixed to 9.2 aW, corresponding to an average number of photons in the probe mode much smaller than one. Indeed, the occupancy of the probe mode from the readout excitation is given by

$$\bar{n}_p^g = \frac{P_r}{\hbar\omega_p^g} \frac{\kappa_p^{\text{cpl}}}{(\kappa_p/2)^2}, \quad (\text{S13})$$

where κ_p is the total linewidth of the probe mode and κ_p^{cpl} is the coupling rate of the cavity input-output port to the probe mode. With values of κ_p^{cpl} and κ_p given in Tables S2, we obtain $\bar{n}_p^g = 0.078 \pm 0.004$ for $P_r = 9.2$ aW.

B. Analytical model

To take into account the finite occupancy of the probe mode for qubit spectra measured with the Kittel mode in the vacuum state ($P_{\text{mw}} = 0$), we use the analytical spectrum $S(\omega_s)$ of equation (S5) by considering the probe cavity mode as the harmonic oscillator through the substitutions

$$\begin{aligned} n, \bar{n}^{g,e}, \kappa &\rightarrow n_p, \bar{n}_p^{g,e}, \kappa_p, \\ \chi &\rightarrow \chi_{q-p}, \\ \Delta_d, \Omega_d &\rightarrow \Delta_p, \Omega_p, \\ A, B, D^{\text{ss}} &\rightarrow A_p, B_p, D_p^{\text{ss}} \end{aligned}$$

in Eqs. (S6) to (S12). This leads to

$$S(\omega_s) = \sum_{n_p=0}^{\infty} \frac{1}{\pi} \frac{1}{n_p!} \text{Re} \left(\frac{(-A_p)^{n_p} e^{A_p}}{\gamma_q^{(n_p)} - i(\omega_s - \omega_q^{(n_p)})} \right) \equiv \sum_{n_p=0}^{\infty} S_{n_p}(\omega_s). \quad (\text{S14})$$

More explicitly, we fit the measured spectrum $\text{Re}(\Delta r)$ to

$$\text{Re}(\Delta r) = \mathcal{A} \sum_{n_p=0}^{10} S_{n_p}(\omega_s) + \text{Re}(\Delta r)_{\text{off}}, \quad (\text{S15})$$

where \mathcal{A} is a conversion factor from $S(\omega_s)$ to $\text{Re}(\Delta r)$, and $\text{Re}(\Delta r)_{\text{off}}$ is an offset of the spectrum from zero. The Fock basis of the probe mode is truncated to $n_p = 10$. The linewidth κ_p of the probe mode is fixed to the value determined from a fit of the spectrum of the probe mode (Table S2), and the readout detuning Δ_r is zero. The fitting parameters are the qubit frequency with the probe mode in the vacuum state, ω_q , the qubit linewidth $\gamma_q(P_s)$ broadened by the spectroscopy microwave excitation of power P_s , the qubit-probe mode dispersive shift χ_{q-p} , the probe mode occupancy \bar{n}_p^g with the qubit in the ground state, the conversion factor \mathcal{A} , and the offset $\text{Re}(\Delta r)_{\text{off}}$.

C. Fit

The measurements and the fits of the qubit spectra for spectroscopy excitation powers P_s of 19 aW and 190 aW are shown in Figs. S3a and S3b. The dispersive shift χ_{q-p} between the qubit and the probe mode is found to be -0.8 ± 0.2 MHz, in excellent agreement with the expected value of -0.73 MHz (Table S4). The power-broadened qubit linewidth $\gamma_q(P_s)$, shown in Fig. S3c, is fitted to

$$\gamma_q(P_s) = \sqrt{\eta P_s + \gamma_q(0)^2}, \quad (\text{S16})$$

where $\eta \equiv (2\Omega_s)^2/P_s$ relates P_s to the Rabi frequency Ω_s , and $\gamma_q(0)$ is the intrinsic qubit linewidth [S5]. The Rabi frequency Ω_s in equation (S4) is estimated from the power-broadened qubit linewidth with

$$\Omega_s = \frac{1}{2} \sqrt{\gamma_q(P_s)^2 - \gamma_q(0)^2}. \quad (\text{S17})$$

From the fit of $\gamma_q(P_s)$ to equation (S16), we find $\gamma_q(0)/2\pi = 0.25_{-0.10}^{+0.07}$ MHz. To obtain this value, we restrict the minimal value of $\gamma_q(P_s)$ in the fit such that the intrinsic linewidth respects the T_1 limit set by $\min[\gamma_q(0)] = 1/T_1$, with $T_1 = 0.63 \pm 0.07$ μs determined in a time-domain measurement. The linewidth $\gamma_q^{(n_p=0)}(0) = \gamma_q(0) + \kappa_p D_p^{\text{ss}}$ in equation (S7), corresponding to the linewidth of the peak with zero photons and broadened through measurement-induced dephasing from the photon occupancy of the probe mode, is 0.57 ± 0.02 MHz. The difference between $\gamma_q(0)$ and $\gamma_q^{(n_p=0)}(0)$ can be explained by an occupancy in the probe mode of $0.20_{-0.09}^{+0.20}$, significantly higher than the expected occupancy from the probe microwave excitation of 0.078 ± 0.004 previously estimated. This indicates a residual occupancy of $0.12_{-0.10}^{+0.21}$, which should result in a linewidth of $0.44_{-0.27}^{+0.54}$ MHz, broadened from the intrinsic linewidth even in the absence of both probe and spectroscopy microwave excitations. This linewidth compares well with the linewidth of 0.51 ± 0.04 MHz calculated with the dephasing time $T_2^* = 0.62 \pm 0.04$ μs determined from Ramsey interferometry in a time-domain measurement (Figs. S3d and S3e). While all microwave excitations are turned off during the free evolution in the Ramsey interferometry measurement, the residual occupancy of the probe cavity mode creates measurement-induced dephasing of the qubit, increasing the linewidth from 0.25 to 0.51 MHz.

VI. QUBIT SPECTROSCOPY - MAGNON COHERENT STATE

A. Analytical model and fit

Figure S4a schematically represents the energy diagram of the qubit-magnon system in the dispersive regime. To fit the spectrum of the transmon qubit measured in this regime with a coherent excitation applied to the Kittel mode ($P_{\text{mw}} > 0$), we use the analytical spectrum $S(\omega_s)$ of equation (S5) by considering the Kittel mode as the harmonic oscillator through the substitutions

$$\begin{aligned} n, \bar{n}^{g,e}, \kappa &\rightarrow n_m, \bar{n}_m^{g,e}, \gamma_m, \\ \chi &\rightarrow \chi_{q-m}, \\ \Delta_d, \Omega_d &\rightarrow \Delta_{\text{mw}}, \Omega_{\text{mw}}, \\ A, B, D^{\text{ss}} &\rightarrow A_m, B_m, D_m^{\text{ss}} \end{aligned}$$

in Eqs. (S6) to (S12). To take into account the ac Stark shift of the qubit frequency by the photons in the probe mode, we substitute

$$\omega_q \rightarrow \omega_q^{(n_p=0)} = \omega_q + B_p, \quad (\text{S18})$$

where the ac Stark shifted qubit frequency with the Kittel mode in the vacuum state, $\omega_q^{(n_p=0)}/2\pi = 7.99156$ GHz, is determined from the fit presented in Fig. S3a. The qubit linewidth with the Kittel mode in the vacuum state is substituted to

$$\gamma_q \rightarrow \gamma_q^{(n_p=0)} = \gamma_q + \kappa_p D_p^{\text{ss}}, \quad (\text{S19})$$

to take into account the increase in the linewidth by measurement-induced dephasing from photons in the probe mode, with $\gamma_q^{(n_p=0)}/2\pi = 0.78$ MHz (Fig. S3c and Table S3). With these substitutions, we fit the qubit spectrum to

$$\text{Re}(\Delta r) = \mathcal{A} \sum_{n_m=0}^{10} S_{n_m}(\omega_s) + \text{Re}(\Delta r)_{\text{off}}, \quad (\text{S20})$$

where, to take into account the asymmetry in the qubit lineshape from the qubit-probe mode dispersive interaction, we consider the one-photon peak of the probe mode with

$$S_{n_m}(\omega_s) \approx S_{n_m, n_p=0}(\omega_s) + \mathcal{B} \times S_{n_m, n_p=1}(\omega_s), \quad (\text{S21})$$

in equation (S20), where

$$\mathcal{B} \equiv \frac{p_{n_p=1}}{p_{n_p=0}} = \int d\omega_s \frac{S_{n_p=1}(\omega_s)}{S_{n_p=0}(\omega_s)}$$

is the relative spectral weight between the one-photon and the zero-photon peaks. From measurements at $P_{\text{mw}} = 0$ (Fig. S3a), we find $\mathcal{B} = 0.03$, which is supposed to be constant in the following analysis. Figure S4b shows an example of the qubit spectrum for a Kittel mode excitation power of 3.1 fW.

The parameters fixed in the fit of the qubit spectrum are the qubit frequency $\omega_q^{(n_p=0)}$, the power-broadened qubit linewidth $\gamma_q^{(n_p=0)}$, the magnon linewidth γ_m , the relative spectral weight \mathcal{B} , the qubit-probe mode dispersive shift χ_{q-p} , and total linewidth κ_p of the probe mode. For each Kittel mode excitation power, the fitting parameters are the qubit-magnon dispersive shift χ_{q-m} (Fig. S4c), the Kittel mode excitation detuning Δ_{mw} (Fig. S4d), the magnon occupancy with the qubit in the ground state, \bar{n}_m^g (Fig. 3d in the main text), the conversion factor \mathcal{A} , and the offset $\text{Re}(\Delta r)_{\text{off}}$ (Fig. S4f). Excitation-power-averaged values of Δ_{mw} and χ_{q-m} , given in Tables S3 and S4 respectively, are discussed in the main text.

From the value of $\Delta_{\text{mw}}/2\pi = -0.38$ MHz, we can estimate the dressed magnon frequency $\omega_m^g/2\pi = (\omega_{\text{mw}} + \Delta_{\text{mw}})/2\pi = 7.94962$ GHz. The Lamb shift $(\omega_m^{\text{bare}} - \omega_m^g)/2\pi = 1.88$ MHz is calculated from diagonalization of the total Hamiltonian $\hat{\mathcal{H}}$ of equation (S1) using parameters of Table S1. This gives a bare magnon frequency $\omega_m^{\text{bare}}/2\pi = 7.95150$ GHz, from which we calculate $|\omega_q^{\text{bare}} - \omega_m^{\text{bare}}|/2\pi = 89$ MHz, much greater than the qubit-magnon coupling strength of 7.79 MHz.

The offset $\text{Re}(\Delta r)_{\text{off}}$ shows a linear scaling with P_{mw} , with $\text{Re}(\Delta r)_{\text{off}}$ set to zero for $P_{\text{mw}} = 0$. The offset appears as a displacement of the reflection coefficient Δr in phase space, indicating an ac Stark shift of the resonant frequency of the probe mode by the occupancy of the Kittel mode. In the detuning-dependent measurement shown in Fig. 2c of the main text, the Kittel mode spectrum is indeed visible through the dispersive interaction between the probe cavity mode and the Kittel mode [S7].

B. Kittel mode excitation

In Fig. 3d of the main text, the magnon occupancy \bar{n}_m^g increases as a function of the Kittel mode excitation power at a rate of 0.342 ± 0.008 magnons per femtowatt. Theoretically, the magnon occupancy \bar{n}_m^g is given by

$$\bar{n}_m^g = \frac{\Omega_{mw}^2}{(\gamma_m/2)^2 + \Delta_{mw}^2}, \quad (\text{S22})$$

with the Kittel mode excitation strength Ω_{mw} given from the input-output theory by

$$\Omega_{mw} = \sqrt{\frac{P_{mw}}{\hbar\omega_{mw}}} \sum_p \sqrt{\kappa_{10p}^{\text{cpl}}} \left[\frac{g_{m,10p}}{\Delta_{m,10p}} + \frac{g_{q-m}g_{q,10p}}{\Delta_{q-m}\sqrt{\Delta_{m,10p}^2 + \kappa_{10p}^2}} \right], \quad (\text{S23})$$

where $\Delta_{m,10p} = \omega_{10p}^{\text{bare}} - \omega_m^{\text{bare}}$, $\Delta_{q-m} = \omega_q^{\text{bare}} - \omega_m^{\text{bare}}$, and $\Delta_{mw} = \omega_m^g - \omega_{mw}$. For a given p , the first term of equation (S23) describes the excitation of the Kittel mode through a virtual excitation in the TE_{10p} cavity mode, while the second term describes the excitation of the Kittel mode through a virtual excitation in the qubit excited by a virtual excitation in the TE_{10p} cavity mode. This leads to a slope of the magnon occupancy \bar{n}_m^g as a function of the excitation power P_{mw} given by

$$\frac{\bar{n}_m^g}{P_{mw}} = \frac{1}{\hbar\omega_{mw}} \frac{1}{(\gamma_m/2)^2 + \Delta_{mw}^2} \left(\sum_p \sqrt{\kappa_{10p}^{\text{cpl}}} \left[\frac{g_{m,10p}}{\Delta_{m,10p}} + \frac{g_{q-m}g_{q,10p}}{\Delta_{q-m}\sqrt{\Delta_{m,10p}^2 + \kappa_{10p}^2}} \right] \right)^2, \quad (\text{S24})$$

Truncating to sum over cavity modes to $p = 3$, we calculate $\bar{n}_m^g/P_{mw} = 0.16_{-0.06}^{+0.12}$ magnons per femtowatt with parameters given in Tables S1 to S3. Additionally, the linewidth and the coupling rate of the TE_{101} cavity mode are $\kappa_{101}/2\pi = 1.39$ MHz and $\kappa_{101}^{\text{cpl}}/2\pi = 0.13$ MHz, respectively. Error bars correspond to extremal values within the 95% confidence interval of $\kappa_{102}^{\text{cpl}} = \kappa_c^{\text{cpl}}$, $\kappa_{103}^{\text{cpl}} = \kappa_p^{\text{cpl}}$, γ_m , and Δ_{mw} . The discrepancy between the experimental and theoretical slopes of $\bar{n}_m^g(P_s)$ of approximately a factor of two is most likely explained by an underestimation of Ω_{mw} as not all excitation channels of the Kittel mode are taken into account.

C. Probability distribution

The probability p_{n_m} of the magnon number state $|n_m\rangle$ is calculated as the relative spectral weight of each component $S_{n_m}(\omega_s)$ of the fitted spectrum $S(\omega_s)$ with

$$p_{n_m} = \int d\omega_s \frac{S_{n_m}(\omega_s)}{S(\omega_s)}, \quad (\text{S25})$$

where

$$S(\omega_s) \approx \sum_{n_m=0}^{10} S_{n_m}(\omega_s),$$

with $S_{n_m}(\omega_s)$ given by equation (S21). As discussed in Ref. [S4], the probability distributions of equation (S25) are to be compared with Poisson distributions of mean D_m^{ss} given by

$$p_{n_m} = \frac{(D_m^{\text{ss}})^{n_m} e^{-D_m^{\text{ss}}}}{n_m!}. \quad (\text{S26})$$

Figure S5 shows the comparison between the Poisson distributions and the probability distributions calculated using equation (S25) with experimentally determined parameters, but with different values of the magnon linewidth γ_m and excitation detuning Δ_{mw} . For $\gamma_m \ll \chi_{q-m}$ ($\gamma_m/2\pi = 0.1$ MHz, Figs. S5a and S5c), the probability distributions given by equation (S25) follow the Poisson distributions, even for a finite excitation detuning Δ_{mw} of -0.38 MHz [S4]. However, for $\gamma_m \sim \chi_{q-m}$ ($\gamma_m/2\pi = 1.3$ MHz, Figs. S5b and S5d), systematic deviations from the Poisson distribution are observed. In that case, despite being in the strong dispersive regime with $|2\chi_{q-m}| > \max[\gamma_q, \gamma_m]$, the qubit does not perfectly probe the probability distribution of the Kittel mode. Error bars in Fig. 3e of the main text are calculated by finding the extremal values of p_{n_m} calculated within the 95% confidence intervals of the fitting parameters \bar{n}_m^g , χ_{q-m} , and Δ_{mw} .

VII. MAGNON KERR NONLINEARITY

Using the Hamiltonian of the hybrid system of equation (S1), we calculate the magnon Kerr coefficient K_m as a function of the bare magnon frequency ω_m^{bare} (Fig. S6a). For $\omega_m^g/2\pi = (\omega_{\text{mw}} + \Delta_{\text{mw}})/2\pi = 7.94962$ GHz at $I = -5.02$ mA, we estimate $K_m/2\pi = -0.12$ MHz. As this coefficient is much smaller than the magnon linewidth of 1.3 MHz, it is not expected to significantly affect the dynamics of the Kittel mode.

However, to understand the effect of this nonzero Kerr coefficient on the behaviour of the magnon occupancy when increasing the Kittel mode excitation power, we consider the effective Hamiltonian of the driven qubit-magnon system in the dispersive regime given by

$$\begin{aligned} \hat{\mathcal{H}}_{\text{q-m}}/\hbar = & \frac{1}{2}\Delta_s\hat{\sigma}_z + (\Delta_{\text{mw}} + \chi_{\text{q-m}} + K_m/2)\hat{c}^\dagger\hat{c} \\ & + \chi_{\text{q-m}}\hat{\sigma}_z\hat{c}^\dagger\hat{c} - (K_m/2)(\hat{c}^\dagger\hat{c})^2 \\ & + \Omega_s(\hat{\sigma}^- + \hat{\sigma}^+) + \Omega_{\text{mw}}(\hat{c} + \hat{c}^\dagger), \end{aligned} \quad (\text{S27})$$

where $\Delta_s = \omega_q - \omega_s$ is the spectroscopy detuning, $\Delta_{\text{mw}} = \omega_m^g - \omega_{\text{mw}}$ is the Kittel mode excitation detuning, K_m is the coefficient of the magnon Kerr nonlinearity, Ω_s is the spectroscopy excitation strength (Rabi frequency), and Ω_{mw} is the Kittel mode excitation strength. In equation (S27), the qubit and the Kittel mode are in the frames rotating at the dressed qubit frequency ω_q and the magnon frequency ω_m^g , respectively.

By projecting $\hat{\mathcal{H}}_{\text{q-m}}$ of equation (S27) into the $\hat{\sigma}_z \rightarrow -1$ subspace (qubit in the ground state), we obtain the Hamiltonian of a driven Kittel mode with a Kerr nonlinearity

$$\hat{\mathcal{H}}_m/\hbar = (\Delta_{\text{mw}} + K_m/2)\hat{c}^\dagger\hat{c} - (K_m/2)(\hat{c}^\dagger\hat{c})^2 + \Omega_{\text{mw}}(\hat{c} + \hat{c}^\dagger). \quad (\text{S28})$$

Using Qutip [S8, S9], we numerically calculate the steady-state magnon occupancy \bar{n}_m^g with this Hamiltonian and under magnon relaxation at a rate $\gamma_m/2\pi = 1.3$ MHz, as a function of the Kittel mode excitation strength Ω_{mw} . The Kittel mode excitation detuning Δ_{mw} is fixed to zero and -0.38 MHz in Figs. S6b and S6c, respectively. At zero detuning ($\Delta_{\text{mw}} = 0$), a nonzero Kerr coefficient leads to negative curvature in $\bar{n}_m^g(\Omega_{\text{mw}}^2)$ as the excitation gets less efficient when the excitation strength increases, as the increasing magnon occupancy effectively change the excitation detuning for $|K_m| > 0$. However, for a finite detuning of -0.38 MHz, the curvature is positive at small \bar{n}_m^g for a finite range of Kerr coefficients $K_m < 0$. Indeed, in this case, the Kerr nonlinearity compensate the finite detuning, making the Kittel mode excitation more efficient as the magnon occupancy increases. For larger values of \bar{n}_m^g , the curvature becomes negative, as shown in the inset of Fig. S6c.

We now compare the numerically calculated $\bar{n}_m^g(\Omega_{\text{mw}}^2)$ to the data $\bar{n}_m^g(P_{\text{mw}})$ of Fig. 3d in the main text. Figures S6d and S6e shows the coefficient of determination R^2 between $\bar{n}_m^g(\Omega_{\text{mw}}^2)$ and $\bar{n}_m^g(P_{\text{mw}})$ for different values of the Kerr coefficient K_m and the proportionally constant between Ω_{mw}^2 and P_{mw} . Maximizing the coefficient of determination R^2 , we determine a Kerr coefficient K_m of $-0.20_{-0.14}^{+0.05}$ MHz for $\Delta_{\text{mw}}/2\pi = -0.38$ MHz. Error bars on K_m are calculated by finding the extremal values found within the 95% confidence interval of γ_m and Δ_{mw} . Even if the magnon Kerr coefficient is much smaller than the magnon linewidth, the value found from the fit is in relatively good agreement with the value of -0.12 MHz in Fig. S6a. Finally, no thermal occupancy of the Kittel mode is found within our error bars of about 0.01 magnons, indicating an effective magnon temperature smaller than ~ 80 mK.

* yasunobu@qc.rcast.u-tokyo.ac.jp

- [S1] Tabuchi, Y. *et al.* Coherent coupling between a ferromagnetic magnon and a superconducting qubit. *Science*, **349**, 405-408 (2015).
- [S2] Tabuchi, Y. *et al.* Quantum magnonics: The magnon meets the superconducting qubit. *Comptes Rendus Physique*, **17**, 729-739 (2016).
- [S3] Koch, J. *et al.* Charge-insensitive qubit design derived from the Cooper pair box. *Phys. Rev. A*, **76**, 042319 (2007).
- [S4] Gambetta, J. *et al.* Qubit-photon interactions in a cavity: Measurement-induced dephasing and number splitting. *Phys. Rev. A*, **74**, 042318 (2006).
- [S5] Schuster, D. I. *et al.* ac Stark shift and dephasing of a superconducting qubit strongly coupled to a cavity field. *Phys. Rev. Lett.*, **94**, 123602 (2005).
- [S6] Reed, M.D. *et al.* High-fidelity readout in circuit quantum electrodynamics using the Jaynes-Cummings nonlinearity. *Phys. Rev. Lett.*, **105**, 173601 (2010).
- [S7] Haigh, J. A., Lambert, N. J., Doherty, A. C., and Ferguson, A. J. Dispersive readout of ferromagnetic resonance for strongly coupled magnons and microwave photons. *Phys. Rev. B*, **91**, 104410 (2015).

- [S8] Johansson, J.R., Nation, P.D. & Nori, F. QuTiP: An open-source Python framework for the dynamics of open quantum systems. *Comput. Phys. Commun.*, **183**, 1760-1772 (2012).
- [S9] Johansson, J.R., Nation, P.D. & Nori, F. QuTiP 2: A Python framework for the dynamics of open quantum systems. *Comput. Phys. Commun.*, **184**, 1234-1240 (2013).

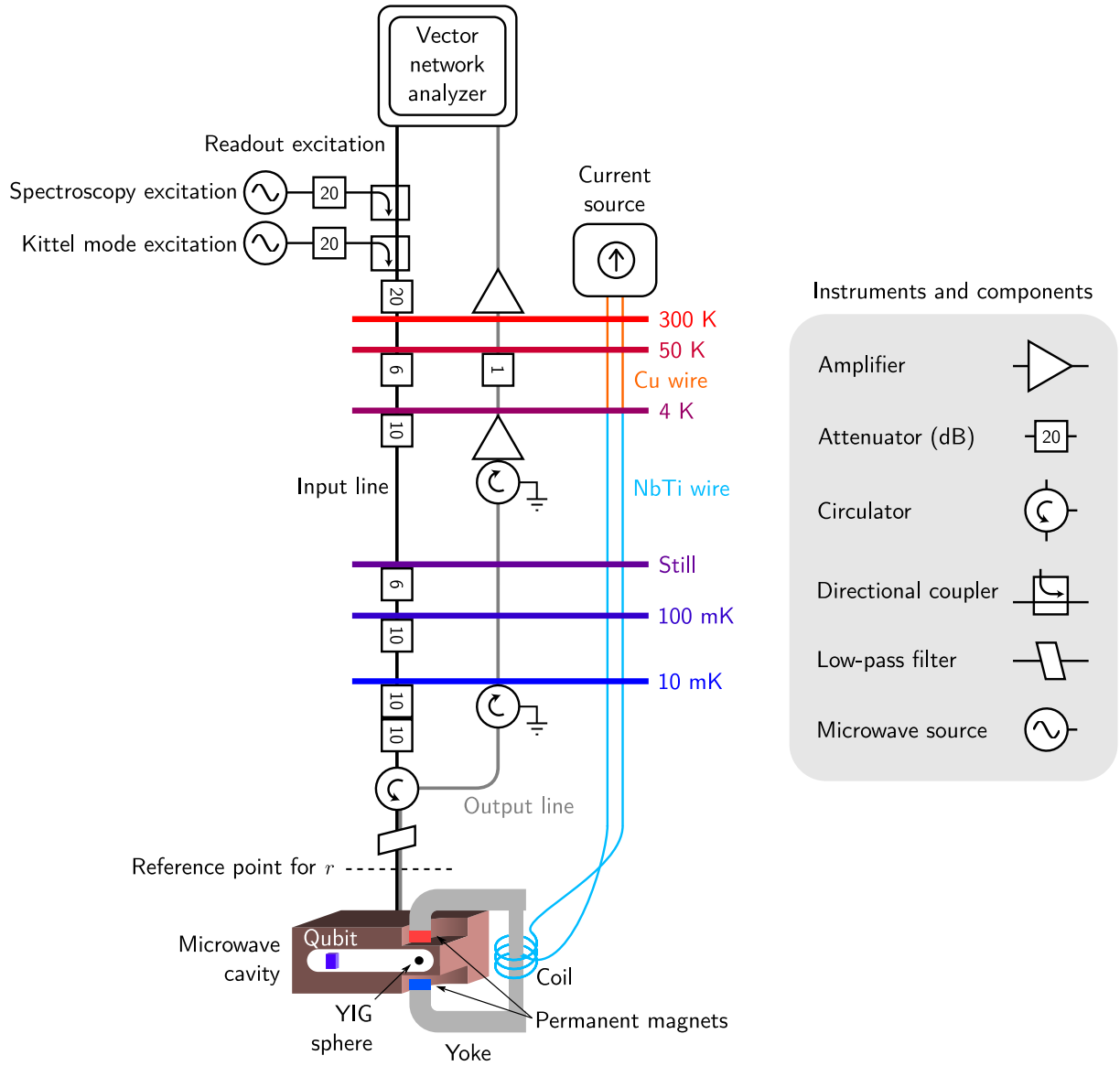


Figure S1. Experimental setup. Spectroscopic measurements are performed with a vector network analyzer (Agilent E5071C). The microwave excitations are generated by microwave sources (Agilent E8247C), combined with the readout microwave excitation from the vector network analyzer in directional couplers (Krytar 120420), and introduced to the input port of the dilution refrigerator. The reflected signal from the cavity is amplified by amplifiers at 4 K (Caltech CRYO4-12) and at room temperature (MITEQ AFS4-08001200-09-10P-4). A current source (Yokogawa GS200) is used to supply the current I to the coil through Cu wires (orange) and superconducting NbTi wires (pale blue). The attenuation of the input line (black) in the dilution refrigerator, of about 59 dB at 10 GHz including losses in cables (phosphor-bronze coaxial cables; Coax Corp. SC-119/50-PBC- PBC) and connectors, is to prevent room-temperature thermal noise from reaching the hybrid system. A low-pass filter at 12 GHz (RLC F-30-12.4-R) is used to further decrease noise into the cavity. Noise from the room-temperature environment and the amplifiers in the output line (grey) are attenuated by more than 60 dB by a circulator (Quinstar XTE0812KCS) and two isolators (Quinstar XTE0812KCS and XTE0812KC). A superconducting NbTi coaxial cable is used in the output line between the two isolators.

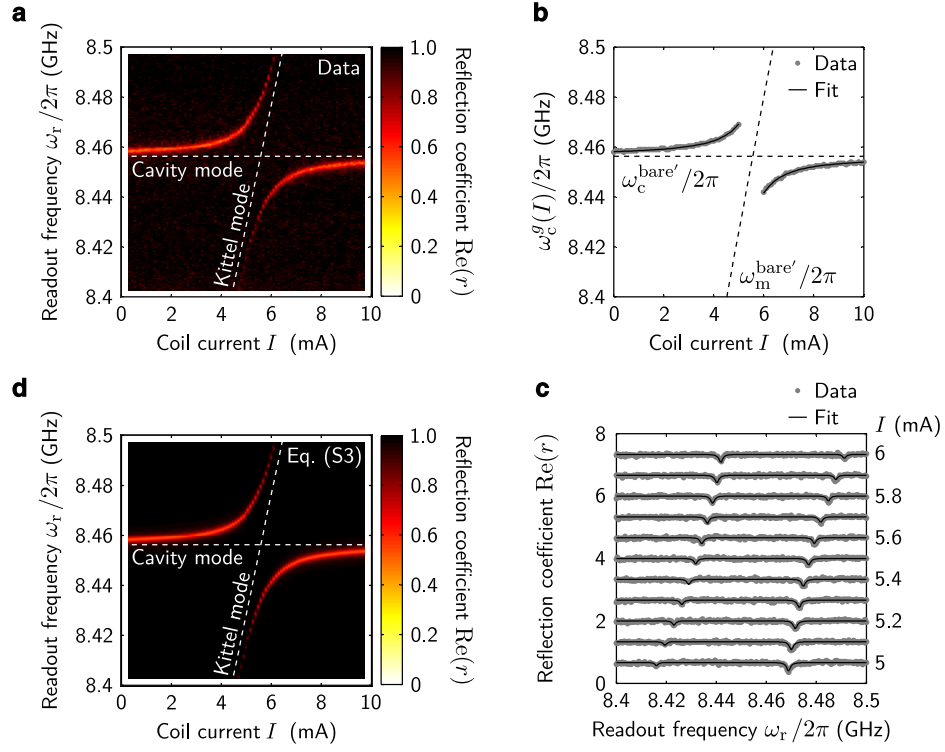


Figure S2. Cavity-magnon coupling. **a**, Measurement of the reflection coefficient $\text{Re}(r)$ of a readout microwave excitation at frequency ω_r as a function of the coil current I . Both the spectroscopy and Kittel mode microwave excitations are turned off for this measurement. The avoided crossing in the coupler cavity mode spectrum indicates the coherent interaction between this cavity mode and the Kittel mode. **b**, Fit of the dressed frequency of the coupler cavity mode with the qubit in the ground state, $\omega_c^g(I)$, to equation (S2). **c**, Fit of the coupler cavity mode spectrum to equation (S3) for different coil currents near the avoided crossing ($I = 5$ to 6 mA). Individual spectra are offset vertically by $\text{Re}(r) = 1$ for clarity. **d**, Coupler cavity mode spectrum as a function of I calculated using equation (S3) with $g_{m-c}/2\pi = 22.5$ MHz and $\gamma_m/2\pi = 1.3$ MHz. For **a**, **b** and **d**, coupler and Kittel modes frequencies bare of their mutual interaction, $\omega_c^{\text{bare}'}$ and $\omega_m^{\text{bare}'}$ respectively, are shown as horizontal and diagonal dashed lines.

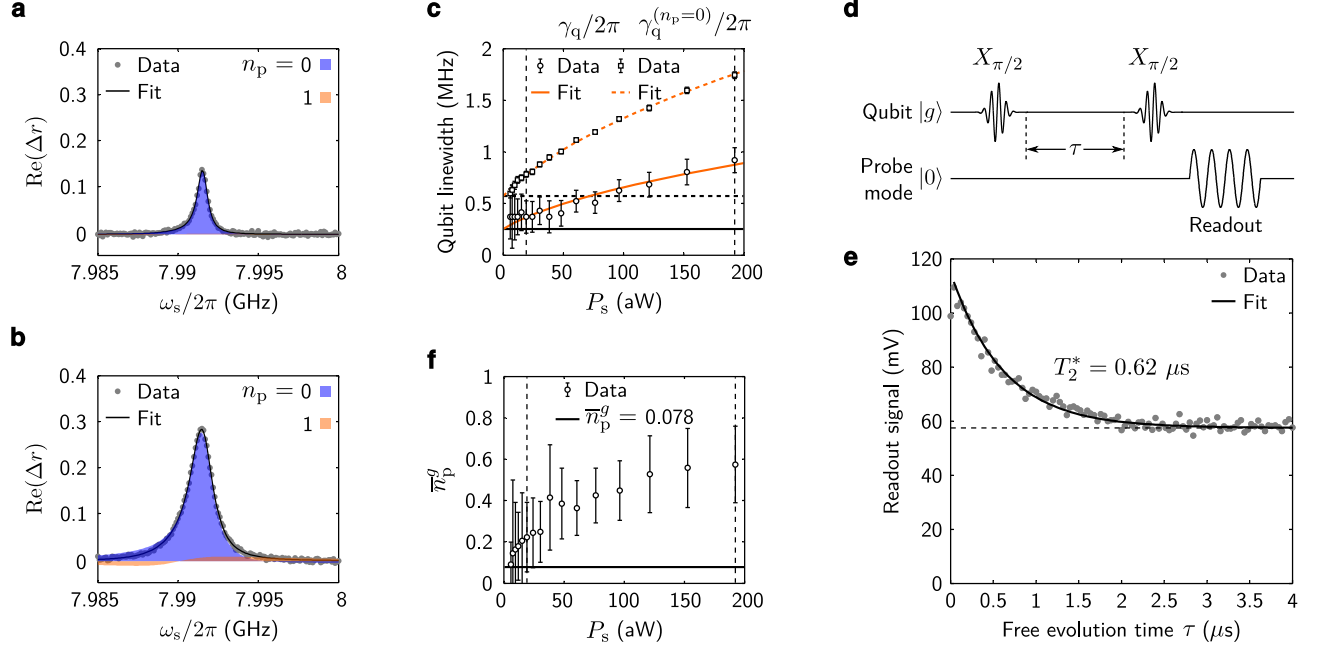


Figure S3. Power broadening of the qubit spectrum. **a, b**, Qubit spectra for spectroscopy excitation powers P_s of **a**, 19 aW and **b**, 190 aW. Fits of data to equation (S15) are shown as black lines. Blue and orange shaded areas respectively show the peaks corresponding to zero and one photons in the probe cavity mode. Note that the asymmetry in the qubit lineshape is very well reproduced by the fit. **c**, Power-broadened qubit linewidths γ_q (circles) and $\gamma_q^{(n_p=0)}$ (squares) in equation (S7) as a function of P_s . Solid and dashed orange lines show fits to equation (S16), indicating linewidths $\gamma_q(0)/2\pi = 0.25$ MHz (horizontal black solid line) and $\gamma_q^{(n_p=0)}(0)/2\pi = 0.57$ MHz (horizontal black solid line) for $P_s \rightarrow 0$. **d**, Pulse sequence used to measure the qubit dephasing time T_2^* with Ramsey interferometry. An initial $\pi/2$ pulse prepares the qubit in a coherent superposition between the $|g\rangle$ and $|e\rangle$ states. After a time τ during which the qubit evolves freely, a second $\pi/2$ pulse is applied to the qubit. In the frame rotating at the qubit frequency, these two pulses would ideally result in the qubit in the excited state. In the presence of dephasing, the probability of finding the qubit in the excited state decays on a timescale given by the dephasing time T_2^* . Readout is performed by sending a strong microwave pulse resonant with the probe mode [S6]. **e**, Readout signal as a function of the free evolution time τ between the two $\pi/2$ pulses. From the fit, we extract $T_2^* = 0.62 \mu\text{s}$. The zero of the readout signal is defined as the signal with the qubit in the ground state, such that the readout signal is proportional to the probability p_e of finding the qubit in the excited state after the pulse sequence shown in **d**. **f**, Occupancy of the probe cavity mode as a function of P_s . Horizontal solid line shows the occupancy $\bar{n}_p^g = 0.078$ calculated with equation (S13). For **c** and **f**, vertical dashed lines show $P_s = 19$ aW and 190 aW.

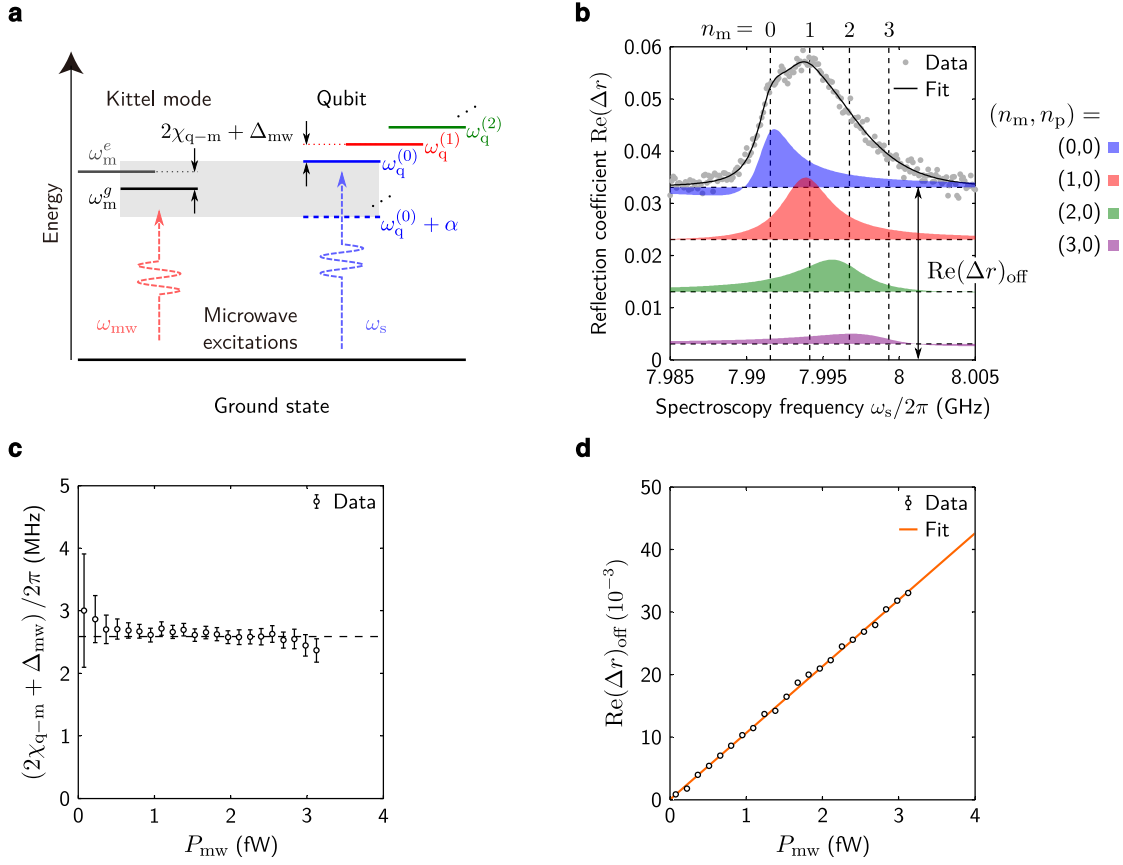


Figure S4. Dispersive qubit-magnon interaction. **a**, Schematic energy diagram for the qubit and the Kittel mode in the dispersive regime, indicating the transitions $|g\rangle \leftrightarrow |e\rangle$ and $|e\rangle \leftrightarrow |f\rangle$ of the transmon at frequencies $\omega_q^{(n_m)}$ and $\omega_q^{(n_m)} + \alpha$ respectively, where $\alpha (< 0)$ is the transmon anharmonicity and $|n_m = \{0, 1, 2, \dots\}\rangle$ are the magnon number states. The straddling regime corresponds to $\omega_q^{(0)} + \alpha < \omega_m^g < \omega_q^{(0)}$ (shaded area), where $\omega_m^{g(e)}$ is the magnon frequency with the qubit in the ground (excited) state $|g(e)\rangle$. A microwave excitation at ω_{mw} is used to drive the Kittel mode at a detuning $\Delta_{mw} = \omega_m^g - \omega_{mw}$, leading to a splitting of $2\chi_{q-m} + \Delta_{mw}$ between qubit transitions corresponding to successive magnon number states. **b**, Qubit spectrum for $P_{mw} = 3.1$ fW and the corresponding fit (black line). Color-coded shaded areas show components of the spectrum corresponding to different magnon number states $|n_m\rangle$ and probe mode in the vacuum state $|n_p = 0\rangle$. Components of the spectrum corresponding to one photon in the probe mode are not clearly visible and are therefore not shown. Components corresponding to $|n_m = \{1, 2, 3\}\rangle$ are offset vertically by -0.01 , -0.02 and -0.03 , respectively, from the spectrum offset $\text{Re}(\Delta r)_{\text{off}}$. Negative values in the spectrum component corresponding to $n_m = 0$ are visible for $\omega_s/2\pi \lesssim 7.99$ GHz. **c**, Splitting between qubit transitions corresponding to successive magnon number states, $2\chi_{q-m} + \Delta_{mw}$, as a function of the Kittel mode excitation power P_{mw} . At low excitation powers, it is difficult to determine from the splitting of the peaks the dispersive shift χ_{q-m} and the excitation detuning Δ_{mw} independently. We therefore omit data points for $P_{mw} < 0.9$ fW to estimate average values and standard deviations of χ_{q-m} and Δ_{mw} . However, the splitting $2\chi_{q-m} + \Delta_{mw}$ is constant (within error bars) at 2.6 ± 0.3 MHz for all excitation powers. **d**, Offset $\text{Re}(\Delta r)_{\text{off}}$ as a function of the Kittel mode excitation power P_{mw} . The orange solid line shows a linear fit of $\text{Re}(\Delta r)_{\text{off}}$. In **c** and **d**, error bars indicate 95% confidence intervals. In **d**, error bars are smaller than the symbols.

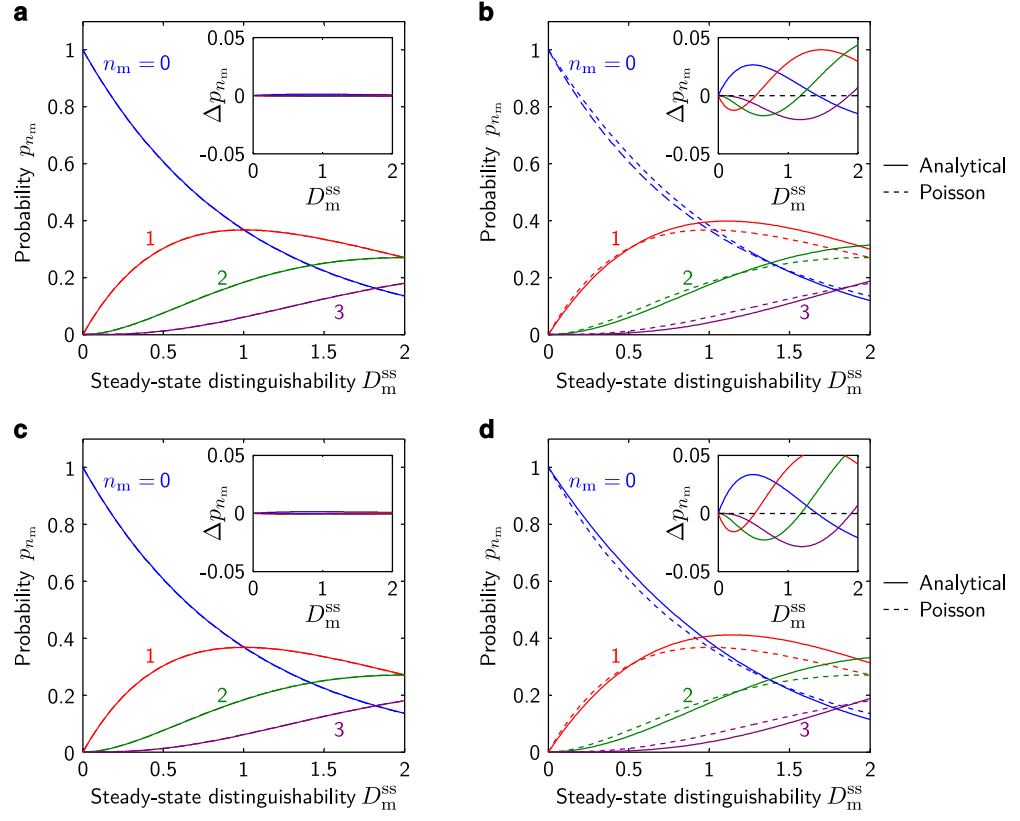


Figure S5. Probability distributions of magnon number states calculated with equation (S25) (solid lines) and equation (S26) (Poisson distribution, dashed lines) for **a**, $\gamma_m/2\pi = 0.1$ MHz and $\Delta_{mw} = 0$, **b**, $\gamma_m/2\pi = 1.3$ MHz and $\Delta_{mw} = 0$, **c**, $\gamma_m/2\pi = 0.1$ MHz and $\Delta_{mw}/2\pi = -0.38$ MHz, and **d**, $\gamma_m/2\pi = 1.3$ MHz and $\Delta_{mw}/2\pi = -0.38$ MHz. Insets show deviations Δp_{n_m} from Poisson distributions.

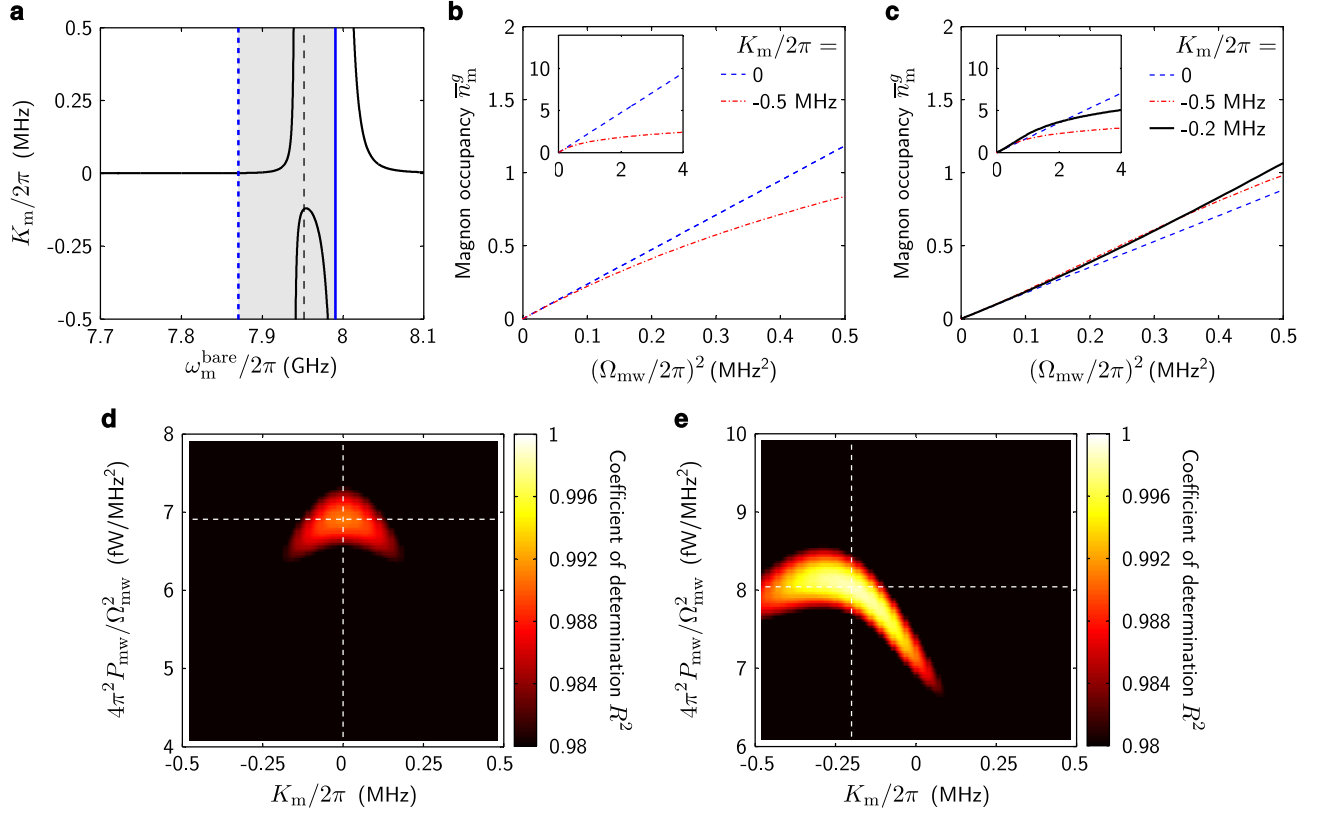


Figure S6. Magnon Kerr nonlinearity. **a**, Calculation of the magnon Kerr coefficient K_m as a function of the bare magnon frequency ω_m^{bare} using the parameters of Table S1. Vertical black dashed line show $\omega_m^{\text{bare}}/2\pi = 7.95150$ GHz, calculated from the experimentally determined $\omega_m^g/2\pi = 7.94962$ GHz and the calculated Lamb shift $(\omega_m^{\text{bare}} - \omega_m^g)/2\pi = 1.88$ MHz. The transmon qubit $|g\rangle \leftrightarrow |e\rangle$ and $|e\rangle \leftrightarrow |f\rangle$ dressed transition frequencies are shown as vertical solid and dashed blue lines, respectively. For a magnon frequency between these two frequencies, the qubit-magnon system is in the straddling regime (shaded area). **b**, **c**, Numerical calculation of the magnon occupancy \bar{n}_m^g as a function of the Kittel mode excitation power, proportional to Ω_{mw}^2 , using the Hamiltonian of equation (S28) for different values of K_m . The magnon linewidth γ_m is 1.3 MHz, and the Kittel mode excitation detuning Δ_{mw} is zero in **b** and -0.38 MHz in **c**. Insets show a larger range of Kittel mode excitation power. **d**, **e**, Coefficient of determination R^2 between $\bar{n}_m^g(P_{\text{mw}})$ (data, Fig. 3 in the main text) and $\bar{n}_m^g(\Omega_{\text{mw}})$ (simulations, this figure) as a function of K_m and the proportionality constant between P_{mw} and Ω_{mw}^2 . The Kittel mode excitation detuning Δ_{mw} is zero in **d** and -0.38 MHz in **e**. Vertical and horizontal dashed lines show best fit values of K_m and $4\pi P_{\text{mw}}/\Omega_{\text{mw}}^2$, respectively.

Parameter	Symbol	Value (MHz)
TE ₁₀₁ cavity mode bare frequency	$\omega_{101}^{\text{bare}}/2\pi$	6994.0
TE ₁₀₂ cavity mode bare frequency	$\omega_{102}^{\text{bare}}/2\pi = \omega_c^{\text{bare}}/2\pi$	8414.5
TE ₁₀₃ cavity mode bare frequency	$\omega_{103}^{\text{bare}}/2\pi = \omega_p^{\text{bare}}/2\pi$	10,441.5
TE ₁₀₄ cavity mode bare frequency	$\omega_{104}^{\text{bare}}/2\pi$	(12,800)
Transmon bare $ g\rangle \leftrightarrow e\rangle$ transition frequency	$\omega_q^{\text{bare}}/2\pi$	8040.6
Transmon bare anharmonicity	$\alpha^{\text{bare}}/2\pi$	-137.2
TE ₁₀₁ cavity mode-qubit coupling rate	$g_{q,101}/2\pi$	73
TE ₁₀₂ cavity mode-qubit coupling rate	$g_{q,102}/2\pi = g_{q-c}/2\pi$	126.1
TE ₁₀₃ cavity mode-qubit coupling rate	$g_{q,103}/2\pi = g_{q-p}/2\pi$	135.4
TE ₁₀₄ cavity mode-qubit coupling rate	$g_{q,104}/2\pi$	(116)
TE ₁₀₁ cavity mode-Kittel mode coupling rate	$g_{m,101}/2\pi$	(-13.6)
TE ₁₀₂ cavity mode-Kittel mode coupling rate	$g_{m,102}/2\pi = g_{m-c}/2\pi$	22.5
TE ₁₀₃ cavity mode-Kittel mode coupling rate	$g_{m,103}/2\pi = g_{m-p}/2\pi$	(-20.3)
TE ₁₀₄ cavity mode-Kittel mode coupling rate	$g_{m,104}/2\pi$	(14.0)

Table S1. Parameters of the hybrid system used for the calculation of the qubit-magnon coupling strength g_{q-m} , the qubit-probe mode dispersive shift $\chi_{q,103} = \chi_{q-p}$, the qubit-magnon dispersive shift χ_{q-m} , and the magnon Kerr coefficient K_m . Parameters in parentheses are numerically estimated based on electromagnetic field simulations.

Parameter	Symbol	Value (MHz)	Figure
Coupler cavity mode linewidth	$\kappa_c/2\pi$	2.08 ± 0.02	
Coupler cavity mode internal loss rate	$\kappa_c^{\text{int}}/2\pi$	1.58 ± 0.02	-
Coupling rate to the coupler cavity mode	$\kappa_c^{\text{cp1}}/2\pi$	0.51 ± 0.02	-
Probe cavity mode linewidth	$\kappa_p/2\pi$	3.72 ± 0.03	-
Probe cavity mode internal loss rate	$\kappa_p^{\text{int}}/2\pi$	2.45 ± 0.03	-
Coupling rate to the probe cavity mode	$\kappa_p^{\text{cp1}}/2\pi$	1.27 ± 0.03	-
Intrinsic qubit linewidth	$\gamma_q(0)/2\pi$	$0.25_{-0.10}^{+0.07}$	S3c
Kittel mode linewidth	$\gamma_m/2\pi$	1.3 ± 0.3	S2

Table S2. Linewidths of the hybrid system. Figures in Supplementary Information related to the parameters are indicated when available. Error bars indicate 95% confidence intervals.

Parameter	Symbol	Value in Fig. 1	Value in Fig. 2	Value in Fig. 3	Figure
Readout excitation power	P_r	9.2 aW			-
Readout excitation frequency	$\omega_p/2\pi$	10.44916 GHz			-
Probe mode occupancy	\bar{n}_p^g	0.6 ± 0.2		0.22 ± 0.17	S3f
Spectroscopy excitation power	P_s	190 aW		19 aW	-
Broadened qubit linewidth	$\gamma_q^{(n_p=0)}(P_s)/2\pi$	1.74 ± 0.04 MHz		0.78 ± 0.03 MHz	S3c
Kittel mode excitation power	P_{mw}	-	7.9 fW	[0.079, 3.1] fW	-
Kittel mode excitation detuning	$\Delta_{mw}/2\pi$	-	[-10.38, 4.62] MHz	-0.38 ± 0.08 MHz	S4c

Table S3. Experimental parameters of the measurements presented in the figures of the main text. Figures in Supplementary Information related to the parameters are indicated when available. Error bars indicate 95% confidence intervals.

Parameter	Symbol	Value (MHz)		Error (%)	Figure
		Experimental	Theoretical		
Qubit-magnon coupling strength	$g_{q-m}/2\pi$	7.79	6.67	+17	1
Qubit-probe mode dispersive shift	$\chi_{q-p}/2\pi$	-0.8 ± 0.2	-0.73	+7	S3
Qubit-magnon dispersive shift	$\chi_{q-m}/2\pi$	1.5 ± 0.1	1.27	+18	2, 3 and S4c
Magnon Kerr coefficient	$K_m/2\pi$	$-0.20^{+0.09}_{-0.13}$	-0.12	+58	S6

Table S4. Comparison between experimental and theoretical values, respectively determined from measurements and from diagonalization of the total Hamiltonian $\hat{\mathcal{H}}$ of equation (S1) using parameters of Table S1. The qubit-probe mode dispersive shift χ_{q-p} , the qubit-magnon dispersive shift χ_{q-m} , and the magnon Kerr coefficient K_m are evaluated at $\omega_{\text{m}}^g/2\pi = (\omega_{\text{mw}} + \Delta_{\text{mw}})/2\pi = 7.94962$ GHz for $I = -5.02$ mA.